

Study on the Impact of Cross-Talk in the ATLAS Electromagnetic Calorimeter on the Signal Prediction in the Strip Layer

Master Advanced Studies (MAS) Thesis by *Ahmed Aly ABDELALIM*

Under the direction of *Prof. Alain Blondel*

June 2006 - September 2008



**UNIVERSITÉ
DE GENÈVE**

Département de Physique Nucléaire et Corpusculaire
Université de Genève

Abstract

The Liquid Argon (LAr) Calorimeters play a central role in the ATLAS detector at the LHC. They measure electrons and photons with high resolution and detect hadronic jets and missing energy signatures.

This thesis is dedicated to study the electronic calibration of the electromagnetic barrel calorimeter, which is a lead-liquid argon sampling calorimeter. ATLAS LAr calorimeters have a special electronic calibration system that injects and measures well known current pulses on the detector cells. This procedure leads to well predicted and calibrated pulses of physics signals.

The effect of capacitive cross-talk between the front compartment (strips) of the LAr calorimeter is considerably high, the strip-strip peak to peak capacitive cross-talk is about 7.2 % and 0.81 % for 1st neighbor strip and 2nd neighbor strip, respectively [29]. A mathematical model which expresses the effects of the capacitive cross-talk is derived. The effect of capacitive cross-talk on the pulse prediction is analyzed. The relative change in the energy content of a single cell, ($\Delta E/E$), is found to be around 0.3 % for a 10% relative cross-talk capacitance.

To my parents...

Contents

Abstract	i
Contents	iv
List of Figures	vi
List of Tables	viii

1. The ATLAS detector	1
1.1 The Large Hadron Collider	1
1.1.1 Physics motivation	2
1.2 The ATLAS Detector	3
1.2.1 Overview	3
1.2.2 The Inner Detector	3
1.2.3 Calorimeters	4
1.2.3.1 The Electromagnetic Calorimeter	4
1.2.3.2 The Hadronic Calorimeters	5
1.2.3.3 The Forward Calorimeter	5
1.2.4 The Muon Spectrometer	6
1.2.5 Trigger and DAQ	7
2. ATLAS Electromagnetic Calorimeter	11
2.1 Basic operation	11
2.2 Energy deposited in ATLAS EM	13
2.3 ATLAS Electromagnetic Calorimeter	15
2.3.1 Electromagnetic Barrel Calorimeter (EMB)	15
2.3.2 Barrel presampler (PS)	18
2.4 Signal processing in ATLAS EM calorimeter	19
2.4.1 Electronic installations in the cryostat and feedthroughs	19
2.4.2 Front-End electronics	20
2.5 Calibration system	22
2.6 Back-end electronics	23
3. Energy reconstruction of a single cell	25
3.1 Main principle	25
3.2 Offline software implementation	25
3.3 Ionization signal reconstruction	26
3.3.1 The Optimal Filtering method	26
3.3.2 Alternative methods to compute the ADC peak	26
3.4 The signal peak to energy conversion factor	27
3.4.1 Ramp factors	27
3.4.2 The $F_{DAC \rightarrow \mu A}$ factor	28
3.4.3 Current-to-energy conversion factors	28
3.4.4 Cross talk	29
3.5 Electronics calibration	30
3.5.1 Calibration constants	30
3.5.2 Pedestal runs	30
3.5.3 Ramp runs	31
3.5.4 Delay runs	31
3.6 Energy reconstruction of a single cell	32

3.7 Signal description.....	33
3.7.1 Physics signal.....	33
3.7.2 Calibration signal.....	33
4. Electrical Properties of the EMC	37
4.1 Introduction	37
4.2 Basic detector electrical model	37
4.2.1 Ionization signal prediction.....	38
4.2.2 Extraction of τ_o from the calibration pulse analysis.....	39
4.3 A circuit simulator as electrical detector model.....	40
4.3.1 Capacitive cross-talk effects.....	41
4.3.2 Adding cables.....	44
4.3.3 Estimation of C_x and C_y	46
4.4 Analytical formulation of the capacitive cross-talk effects	48
4.4.1 First order neighboring cells.....	48
4.4.2 Second order neighboring cells.....	53
4.4.3 Measurement of the LC parameter.....	56
4.5 Impact of capacitive cross-talk on a single cell energy measurement.....	57
Conclusion	59
Acknowledgments	59
Bibliography	61

List of Figures

1.1	Layout of the LHC machine.....	1
1.2	ATLAS detector.....	3
1.3	The ATLAS Inner Detector.....	4
1.4	Calorimeters in the ATLAS detector.....	6
1.5	Muon system in ATLAS.....	7
1.6	The three levels of ATLAS trigger.....	8
1.7	Region of interest (RoI).....	8
2.1	The start of an electromagnetic shower.....	11
2.2	Fractional energy loss per radiation length in lead as a function of electron or positron energy. Electron (positron) scattering is considered as ionization when the energy loss per collision is below 0.255 MeV , and as Moller (Bhabha) scattering when it is above.....	12
2.3	Photon total cross sections as a function of energy in carbon (a) and lead (b).....	12
2.4	Example of energy resolution.....	15
2.5	Accordion-shaped absorber with constant gap-size.....	15
2.6	Layers of the electromagnetic calorimeter.....	16
2.7	Signal layer of the ATLAS EMB calorimeter.....	17
2.8	Sketch of a barrel module.....	18
2.9	Photograph of a PS module.....	19
2.10	EMB Cryostat.....	20
2.11	LAr Calorimeter readout chain from the calorimeter cell until.....	21
2.12	Amplitude versus time for triangular ionization signal and of the FEB output signal after bi-polar shaping. Sampling points are shown.....	21
2.13	The electronic calibration system.....	22
2.14	The Readout derive (ROD).....	23
3.1	Signal induced by the drift electrons in LAr.....	28
3.2	Cross-talk measured in module M13.....	30
3.3	Example for ramps in high gain (circles) and medium gain (squares) in a cell of the middle compartment.....	31
3.4	Example for a shaped calibration pulse (black) and the corresponding predicted physics pulse shape (red).....	32
3.5	The calibration board pulser circuit.....	34
4.1	Basic equivalent circuit of the LAr detector readout cell.....	37
4.2	Frequency response for a typical calibration signal for front compartments.....	39
4.3	(a) a typical calibration pulse, (b) frequency response for the calibration signal from front layer.....	40
4.4	(a) Schematic of a cell, (b) rLC resonance curve.....	40
4.5	Schematic of a cell with a capacitive cross talk with just two neighboring cells one on each side.....	41
4.6	Resonance curves for different C_x values in case of only one neighboring cell.....	42
4.7	Resonance curves for different C_y values in case of only one neighboring cell.....	42
4.8	Schematic of a cell with a capacitive cross talk with 4 neighboring cells, 2 on each side.....	43
4.9	Resonance curves for different C_x values in case of 4 neighboring cells (two on each side).....	44
4.10	Resonance curves for different C_y values in case of 4 neighboring cells (two on each side).....	44

4.11 Schematic of a cell with a capacitive cross talk with 2 neighboring cells, one on each side considering the cables effects.....	46
4.12 Resonance curves for 1 st order neighboring cells with and without cross-talk....	46
4.13 Pulsed cell current as a function of C_x when $C_y = 0$	47
4.14 Neighboring cell current as a function of C_x when $C_y = 0$	47
4.15 The percentage of pulsed cell current change as a function of C_x and C_y	47
4.16 The percentage of neighboring cell current change as a function of C_x and C_y	48
4.17 The calibration current circuit with two neighboring cells, one on each.....	49
4.18 $Z_{Cali}^{(1)}$ as a function of frequency.....	50
4.19 The physics current circuit with two neighboring cells, one on each side.....	51
4.20 The calibration current circuit with 4 neighboring cells, two on each side.....	53
4.21 $Z_{Cali}^{(2)}$ as a function of frequency.....	54
4.22 The physics current circuit with 4 neighboring cells, two on each side.....	55
4.23 The relative energy change due to capacitive cross-talk in LAr strips as a function of η_{cell}	58

List of Tables

2.1 lists the properties of the materials used in the construction of the calorimeter.....	16
2.2 EMB layers Granularity.....	17
3.1 I/E values for PS and Accordion.....	29
4. 1 Minima positions in case of 1 st and 2 nd order neighboring cells for different values of C_x and C_y	45
4.2 1st minimum position in case of 1 st order neighboring cells for different values of C_x and $C_y=0$ using the simulator v_o and the approximate solution v_{ox}	57

Chapter 1

The ATLAS Detector

The ATLAS (A Toroidal LHC ApparatuS) detector is one of the two Large Hadron Collider (LHC) general purpose detectors.

1.1 The Large Hadron Collider

The LHC has been completed by the European Organization for Particle Physics, CERN [1, 2]. It will accelerate two oppositely-rotating proton beams with energy of 7 TeV and will bring them in collision with center-of-mass energy of 14 TeV . The design luminosity is about $10^{34}\text{ cm}^{-2}\text{ s}^{-1}$. Both, the energy and the luminosity of the LHC will be higher than any existing hadron collider. The high center-of-mass energy gives access to possible new heavy particles while the high luminosity allows studying rare interactions.

The LHC is installed in a 27 km circumference tunnel, situated between Lake Geneva and the Jura mountains, that was originally constructed for the Large Electron Positron Collider (LEP) collider.

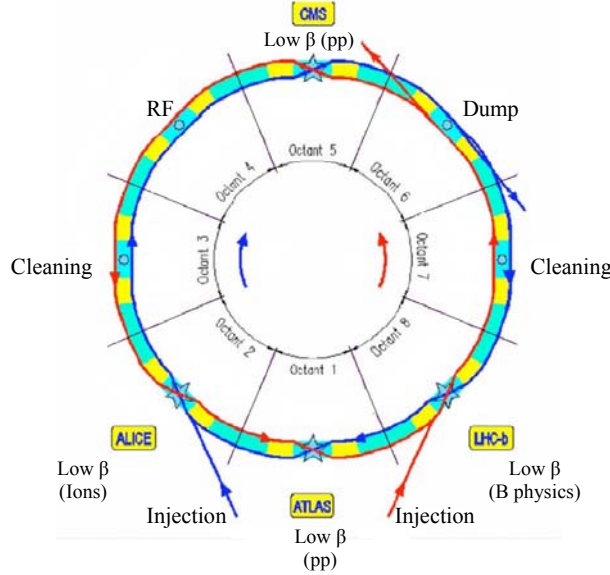


Fig. 1.1: Layout of the LHC machine

The LHC ring (figure 1.1) consists of eight sectors. The central region of each sector is equipped with bending magnets to keep the beam in its orbit. The collision energy of a circulating particle accelerator is determined by its radius and the magnetic bending field. In order to achieve center-of-mass energy of 14 TeV a magnetic field of 8.4 T in the dipole bending magnets is used. To produce such a high magnetic field superconducting magnets are necessary. A total of 1300 superconducting bending dipoles are installed in the LHC. They will be cooled down to $\sim 1.9^\circ\text{ K}$ using superfluid helium. Superfluid helium has a much higher heat transmission capacity and much lower viscosity than in its normal liquid state. Thus, it is possible to work with a lower helium flow. The two beam pipes for the two oppositely-rotating beams are installed in the same cryostat.

Between the bending magnets there are straight sections that comprise: (1) focusing and defocusing quadrupole magnets that keep the particles on track using the alternating gradient principle; (2) the accelerating RF cavities; (3) the beam dump; and (4) the beam cleaning.

At each sector center, the beams are brought to collision. Points 1, 2, 5 and 8 are used for ATLAS, ALICE, CMS, and LHCb experiments respectively. At points 1 and 5 the beam is focused to a small spot that will give the desired high-luminosity. The LHC will also be able to accelerate Pb-ions, with a center-of-mass energy in the PeV range.

1.1.1 Physics motivation

Today, the Standard Model (SM) practically describes all particle physics measurements of the elementary particles of matter and their interactions. It includes three of the four fundamental forces: the strong, the weak, and the electromagnetic forces. The gravitational force is not included in the Standard Model.

Previous experiments (at LEP, Tevatron and other accelerators) found an agreement of the SM with the data up to a precision of 10^{-3} to 10^{-4} . But one important piece of the SM still needs experimental verification: the Higgs mechanism that explains how the point-like particles of the SM acquire their masses. One experimental observation of the Higgs mechanism is the existence of a particle of unknown mass called the Higgs boson [3]. Its lower mass limit is 114.4 GeV which is set by direct searches at LEP [30]. An upper limit of about 1 TeV comes from theory, because the SM can not be consistently formulated with a higher Higgs mass. In order to either discover the Higgs particle or falsify the theory, an accelerator covering this energy range is needed. This was the most important motivation to build the Large Hadron Collider.

However, the SM seems to be incomplete theory. It relies on various input parameters whose values are not explained and it does not provide a theoretical explanation why there are exactly three generations of quarks and leptons. Furthermore, there are experimental indications that neutrinos have mass which has not been accommodated in the Standard Model [4]. Thus theoretical considerations suggest that it is just a low-energy approximation of a more general theory that includes also gravity. LHC might give a hint how this theory has to look like.

The LHC provides also the possibility to measure the properties of already known particles with a better accuracy with its high energy and high luminosity. Many particles (W , Z -bosons, b-quarks, top-quarks ...) will be produced at high rates giving high statistics and thus can be measured accurately [5].

At last, there is a possibility that LHC experiments will discover a completely unexpected physics that is not predicted by any known theory.

1.2 The ATLAS Detector

1.2.1 Overview

ATLAS aims to cover a large possible range of physics expected from LHC. The detector has a cylindrical symmetry around the beam axis. It consists of a barrel part and two end-caps. It is almost perfectly hermetic, leaving only minimal cracks, e.g. between the barrel and the end-caps and the hole of the beam line in the very forward/backward regions. The overall size of the detector is 44 m in length and 25 m in diameter. It has a total weight of 7000 tons [6].

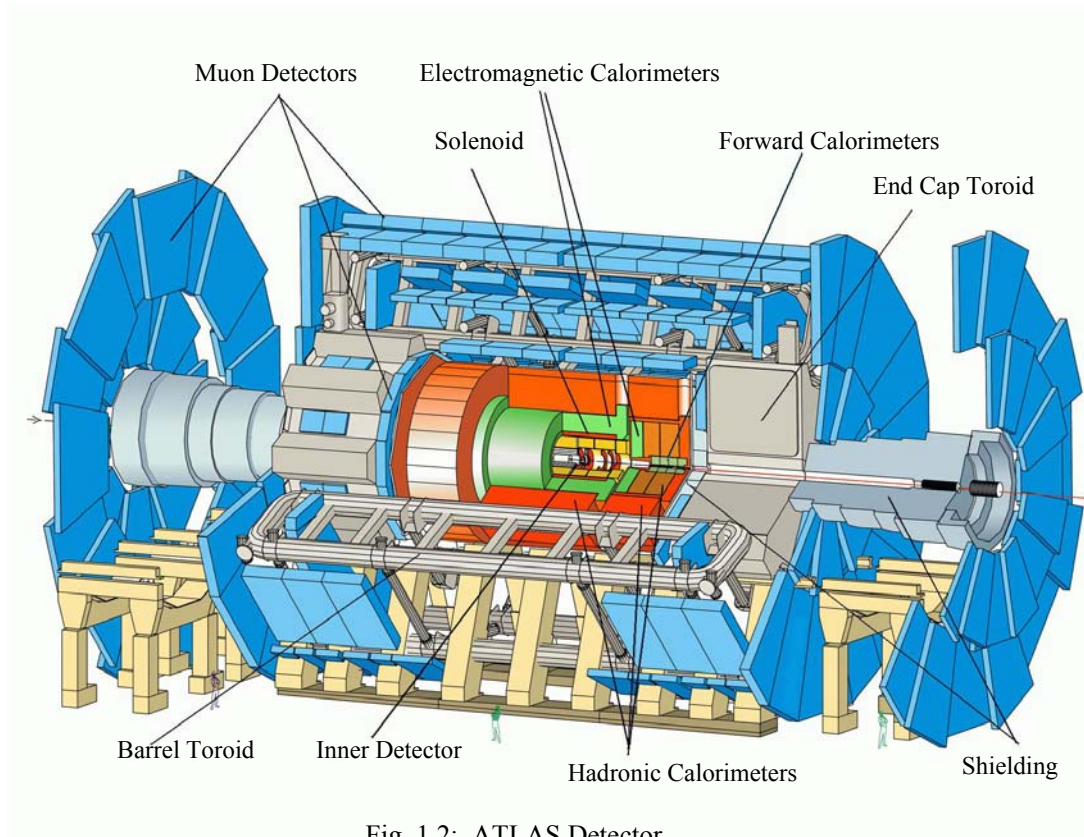


Fig. 1.2: ATLAS Detector

ATLAS (Figure 1.2) consists of several sub-systems arranged as onion-skins. The innermost shell is the Inner Detector followed by the Calorimeters (Electromagnetic and Hadronic) and the Muon Spectrometer.

1.2.2 The Inner Detector

The Inner Detector (ID) (figure 1.3) is used to reconstruct tracks and vertices with high efficiency. It measures the momenta of charged particles through the curvature of their tracks in the B-field and the decay vertices of short lived particles. It contributes, together with the calorimeters and the muon system, to the electron, photon and muon detection. Its acceptance covers the pseudo-rapidity (η) range from -2.5 to 2.5 [7].

The ID consists of high-resolution detectors at inner radii and continuous tracking elements at outer radii, all contained in a 2 T B-Field from the central solenoid. The highest granularity around the vertex region is achieved using semiconductor detectors: a pixel

detector around the interaction point followed by a SemiConductor Tracker (SCT). At least four SCT layers and three pixel layers are crossed by each track. Outside the SCT, a Transition Radiation Tracker (TRT) provides additional tracking capabilities. The TRT has a much lower density than the high precision silicon trackers, keeping the total amount of material in front of the calorimeters small.

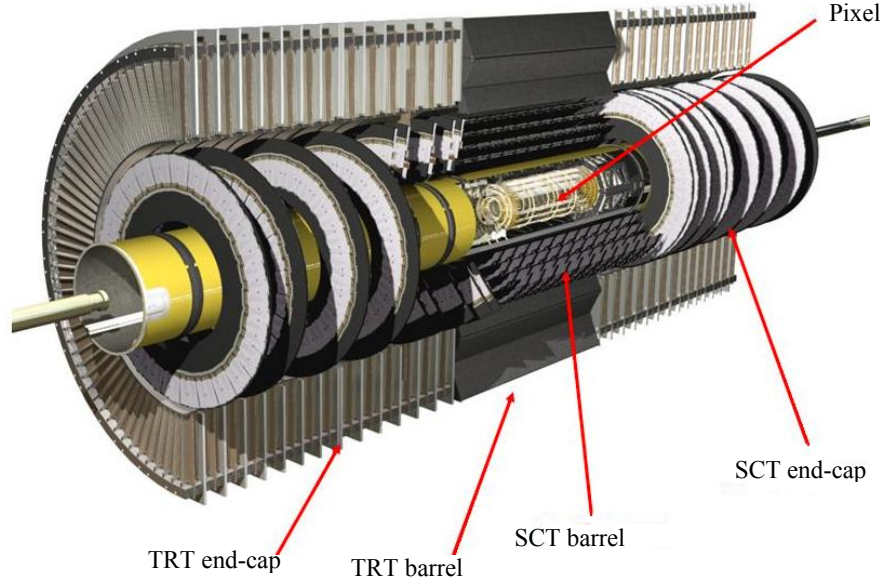


Fig. 1.3: The ATLAS Inner Detector

The outer radius of the tracker cavity is 115 cm and has a total length of 7 m. The precision tracking elements are contained in a radius of 56 cm. Mechanically, the inner detector is subdivided into a barrel part and two identical end-caps.

1.2.3 Calorimeters

Calorimeters are designed to measure the energy and the position of electrons, positrons, photons and jets, to give an estimation of the missing transverse momentum and to contribute to the particle identification [7]. Figure 1.4 shows the Calorimeter system in ATLAS which includes Electromagnetic Calorimeters (EM) and Hadronic Calorimeters. Both of the EM and Hadronic calorimeters consist of a barrel and two end-caps. The forward regions are equipped with a dedicated Forward-Calorimeter (FCAL). All calorimeters used in ATLAS are sampling calorimeters.

1.2.3.1 The Electromagnetic Calorimeter

- Performance

The electromagnetic calorimeter is able to reconstruct electrons in the energy range from 1 GeV up to 5 TeV . The lower limit is set by the requirements for b-tagging. Although, b-tagging is mainly done by the Inner Detector, a calorimetric identification of low-energy electrons increases the b-tagging efficiency by about 10%. The upper energy limit is set by the possibility to produce new heavy gauge bosons (Z' -boson and W' -boson) that appear in

many theories that extend the Standard Model. A large dynamic range guarantees a precise measurement of single cell energy up to 3 TeV [7].

In order to achieve a mass resolution of 1% for the Higgs particle in the decay channels $H \rightarrow \gamma\gamma$ and $H \rightarrow 4e$ an excellent energy resolution and linearity in the range of 10 to 300 GeV is needed. The sampling term should be around $\sim 10\%/\sqrt{E(GeV)}$ and the constant term should not exceed 1% . The linearity in this energy range should be better than 0.5% .

The calorimeters have to cope with the effect of pile-up as well as the high radiation dose due to the unprecedented luminosity of the LHC.

- Construction

While the electromagnetic barrel (EMB) covers η range up to 1.475, the electromagnetic end-caps (EMEC) ranges from 1.375 to 3.2 on both sides. It is constructed from lead absorbers interleaved with liquid argon as active material. The EM will be explained in detail in chapter 2.

1.2.3.2 The Hadronic Calorimeters

- Requirements

The required jet-energy resolution depends on the rapidity region. At $|\eta| \leq 3$, a resolution of $50\%/\sqrt{E(GeV)}$ and a constant term of 3% is necessary. For $|\eta| > 3$, $100\%/\sqrt{E(GeV)}$ and a constant term of 10% is sufficient.

- Construction

- Hadronic Barrel Calorimeter

The Hadronic Barrel Calorimeter has a large steel absorber tiles equipped with scintillating fibers for readout. Therefore, this calorimeter is also called Tile-Calorimeter [7]. Each scintillator is connected to two photomultipliers by wavelength shifting fibers. There is a central barrel part (Tile barrel) covering the η region up to 1.0 and Tile extended barrel on each side that covers η up to 1.7. The gap between the Tile barrel and the Tile extended barrel is used for the cables from the Inner Detector and the EM to outside. Scintillators placed in this gap allow a good estimation of the energy lost in this gap.

- Hadronic End-Cap Calorimeter

The Hadronic end-cap (HEC) uses also the liquid argon as the active medium. The absorbers are flat parallel copper plates. It is placed behind the EMEC in the same cryostat. It covers the η range between 1.5 and 3.2.

1.2.3.3 The Forward Calorimeter

The FCAL provides electromagnetic as well as hadronic calorimetry in the very forward region (η ranges from 3.2 to 4.9). It is located in the inner bore of the hadronic calorimeter

and around the beam pipe. The first of three forward-calorimeter modules use copper as absorber, the other two are made of tungsten. The FCAL has a much thinner active gap compared to the other LAr calorimeters because of the much higher counting rate [7].

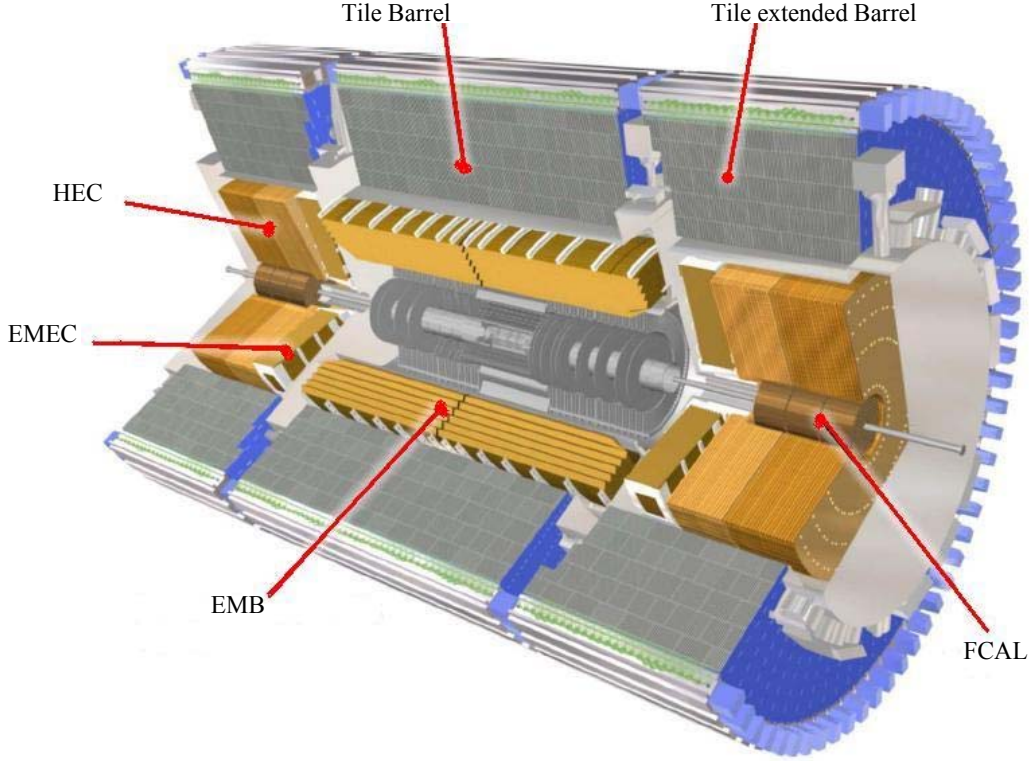


Fig. 1.4: Calorimeters in the ATLAS detector

1.2.4 The Muon Spectrometer

The ATLAS detector is equipped with a high-resolution muon spectrometer [7]. In the barrel region it consists of a large air-core toroidal magnet system, to deflect muon tracks which is needed for momentum measurements, instrumented with Monitored Drift Tube (MDT) chambers to measure the muon trajectory with very high precision in the bending direction and Resistive Plate Chambers (RPC) which provide a stand-alone triggering capability over a wide range of transverse momentum, pseudo-rapidity (η) and azimuthal angle. In the end-cap region, MDTs are also used for muon trajectory and Thin Gap Chambers (TGC) are used as trigger chambers. The very forward region is instrumented with Cathode Strip Chambers (CSC) instead of MDTs to accommodate the higher counting rates.

TGCs have a time resolution better than the 25 ns LHC bunch crossing time spacing, and are used to trigger the acquisition of events with a definite p_T cut-off.

The magnet system provides a field of 0.5 T. Three layers of precision chambers allow the measurement of three points of the muon trajectory. The performance benchmark is to measure the momentum of a 1 TeV muon with a resolution $\frac{\Delta p_T}{p_T} \approx 10\%$. Given the magnetic

field and the available space, this requires a position resolution of $50\text{ }\mu\text{m}$. For $p_T > 6\text{ GeV}/c$, $\frac{\Delta p_T}{p_T} \approx 1\%$ the expected muon identification efficiency is above 90%.

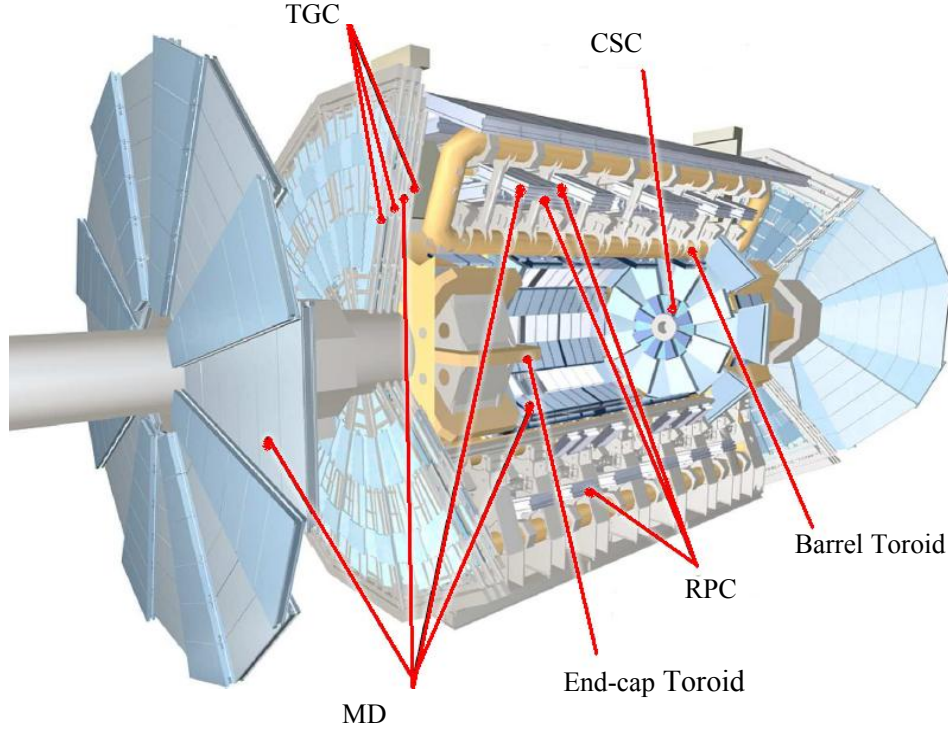


Fig. 1.5: Muon system in ATLAS

1.2.5 Trigger and DAQ

Due to the very high interaction rate in the ATLAS detector, a reliable trigger system is needed that can reduce the huge amount of data. Interesting events are very rare. In 10^7 events only 1 event is selected and recorded for the off-line analysis. The ATLAS trigger and data-acquisition system is based on three levels of online event selection [7], figure 1.6. At LVL1, special-purpose processors act on reduced-granularity data from a subset of the detectors. LVL2 uses full-granularity, full-precision data from the detectors, but, for most triggers, examines only regions of the detector identified by the LVL1 trigger as containing interesting information. At the third trigger level, the event filter (EF), the full event data are used together with the latest available calibration and alignment information to make the final selection of events to be recorded for offline analysis [8].

The LVL1 trigger receives data at 40 MHz (the LHC bunch-crossing rate) providing a decision for each bunch crossing with a latency of $\sim 2\text{ ms}$ during which all detector data are held in pipeline memories. The maximum accept rate of the LVL1 trigger is set at 75 kHz which is determined by the capabilities of the sub-detector readout systems. ATLAS requires that it must be possible to upgrade these systems to operate at 100 kHz with a somewhat higher dead time (a few per cent) and, therefore, the DAQ and LVL2 trigger systems are designed to accept this higher input rate.

Passing LVL1 trigger, data are moved off the detector and stored in readout buffers (ROBs) during the LVL2 trigger processing and the event-builder collection time. The LVL2 trigger reduces the acceptance rate to ~ 1 kHz. It uses the concept of regions of interest (RoIs), figure 1. 7. The LVL1 trigger is used to identify, for each event, regions of the detector containing interesting features such as high- p_T electromagnetic clusters, jets and muons. LVL1 also provides LVL2 with information about global event properties (the total scalar E_T and the missing- E_T vector) and it specifies which signatures led to the event being selected by the LVL1 trigger.

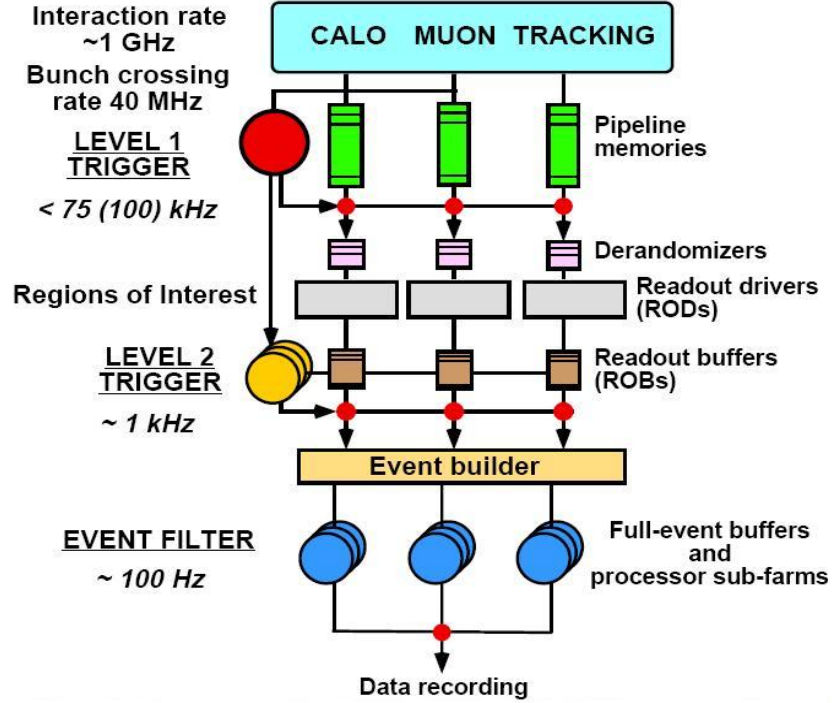


Fig. 1.6: The three levels of ATLAS trigger.

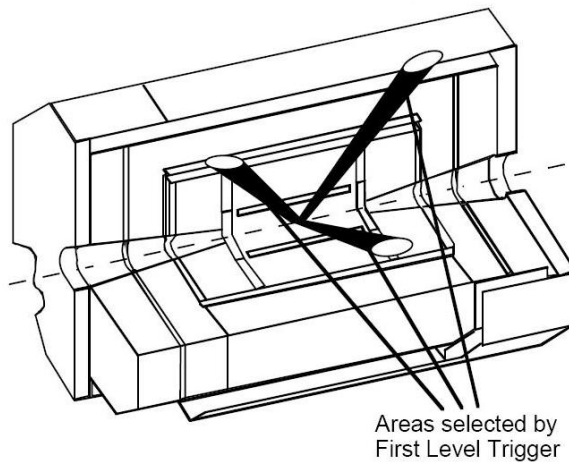


Fig. 1.7: Region of interest (RoI).

The LVL2 trigger uses full-precision information from the inner tracking detectors, the calorimeters and muon detectors. Data from the sub-detectors are combined to provide better particle identification and higher measurement precision than those provided by LVL1. The average decision time for the LVL2 trigger is estimated to be ~ 10 ms [8].

The events accepted by the LVL2 trigger are sent to the EF processors via the event builder. Complete event reconstruction is possible at LVL3 whose decision time is ~ 1 s. The EF system must achieve a data-storage rate of ~ 100 Mbyte/s by reducing the event rate and/or the event size. For some triggers the full event data of about 1 Mbyte will need to be recorded, implying a maximum event rate of 100 Hz, while for others a reduced readout is sufficient, allowing a higher event recording rate.

Chapter 2

The ATLAS Electromagnetic Calorimeter

The ATLAS EM calorimeter is a sampling calorimeter with liquid argon as active material and lead absorbers as the passive material [7]. It consists of a barrel part covering $|\eta| \leq 1.475$ and two end-caps covering η range from 1.375 to 3.2 at both ends. Liquid argon is a radiation hard material that allows fast and linear readout. The lead absorbers make the average density high enough and the radiation length short enough to absorb high-energy electrons and photons in a reasonable depth.

2.1 Basic operation

Electromagnetic showers are produced by particles that interact primarily or exclusively via the electromagnetic force, usually photons and/or electrons. As in figure 2.1, an electromagnetic shower begins when a high-energy electron or photon hits the detector material. At high energy, photons interact with matter primarily via pair production, i.e. they convert into an electron-positron pair, interacting with an atomic nucleus or electron in order to conserve momentum. High-energy electrons and positrons when accelerated or decelerated emit photons, through a process called bremsstrahlung. These two processes continue in turn, until the remaining particles have energies less than the pair production threshold. Electrons and photons then lose energy via scattering until they are absorbed by atoms. Thus the main processes that arise an electromagnetic shower are the following:

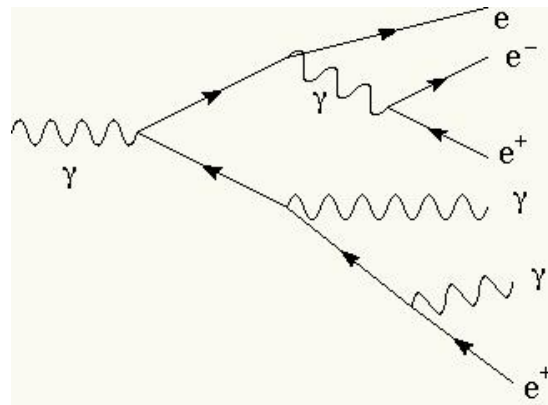


Fig. 2.1: The start of an electromagnetic shower.

1. Bremsstrahlung

At high-energies the main source of loss energy by electrons (positrons) passing through matter is bremsstrahlung resulting from coulomb interactions with the electric field of atomic nuclei. The energy spectrum of the irradiated photons varies as $1/E$. In the limit of very hard bremsstrahlung the entire energy of an electron can be emitted as a photon but this is very rare. In

general, the bremsstrahlung photons carry only a small fraction of the energy of the charged particle. The direction of the initial particle changes slightly during such a process. The energy loss of an electron by bremsstrahlung is approximately proportional to the electron energy (figure 2.2).

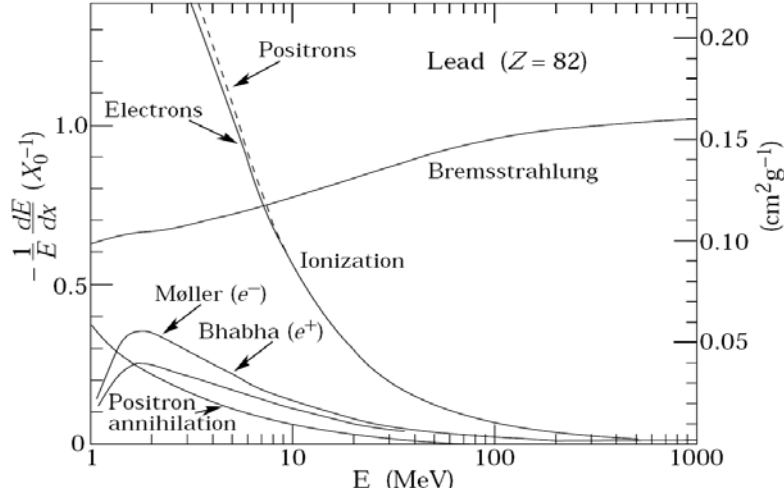


Fig. 2.2: Fractional energy loss per radiation length in lead as a function of electron or positron energy. Electron (positron) scattering is considered as ionization when the energy loss per collision is below 0.255 MeV , and as Møller (Bhabha) scattering when it is above [9].

2. Pair production

Photons with energy of at least twice the electron rest mass can produce an electron-positron pair in the Coulomb field of an atomic nucleus or an electron. The cross-section for this process rises with energy and reaches an asymptotic value at very high energies ($> 1 \text{ GeV}$). For energies above some MeV (depending on the absorber material), pair production becomes the dominant photon interaction process (figure 2.3).

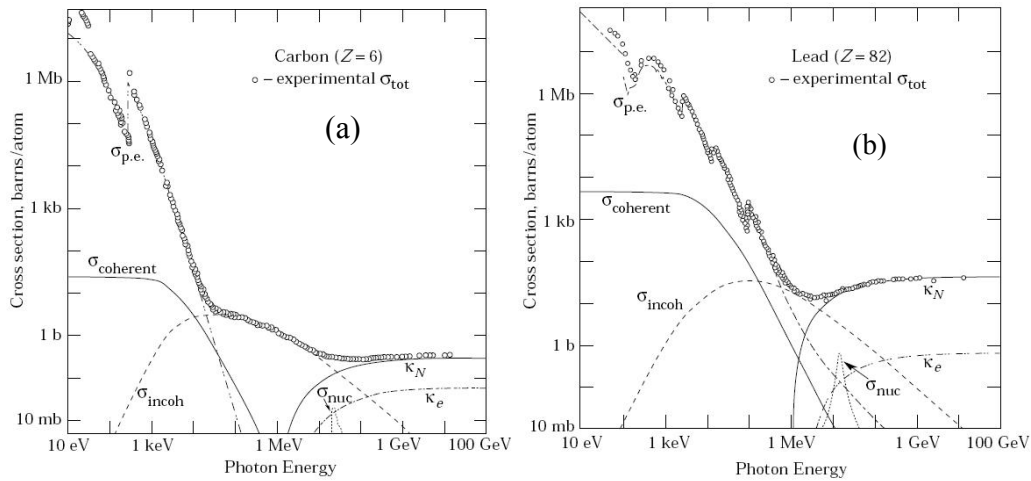


Fig. 2.3: Photon total cross sections as a function of energy in carbon (a) and lead (b) [9]

3. Compton and Rayleigh scattering

Rayleigh scattering is a coherent process; the photon changes its direction by interacting with an atomic electron but does not lose energy. In contrast, a photon that undergoes Compton scattering does transfer part of its energy and momentum to an atomic electron that is put into an unbound state. The process will result in a free electron and a scattered photon. For most absorber materials, Compton scattering is by far the most likely process for photons with energies between a few hundred keV and a few MeV (figure 2.3).

4. Photoelectric effect

At even lower energies, the most likely process is the photoelectric effect, where a photon is absorbed by an atom that in turn emits an electron. The atom is put into an excited state by this process and will return into its ground state by emission of Auger electrons or X-rays. The cross section for the photoelectric effect depends strongly on the electron density and thus on the Z of the absorber material. It scales like Z^n where n is between 4 and 5.

Radiation length

The appropriate scale length to describe the development of an electromagnetic shower is the radiation length X_o which is the mean distance over which an electron loses $1/e$ of its energy by bremsstrahlung. The mean free path for pair-production of a high-energy photon is $7/9$ radiation lengths. Therefore X_o is a characteristic distance for the two processes that develop an electromagnetic shower. X_o in a material is usually measured in g cm^{-2} . It can be approximated by [9]:

$$X_o = \frac{A}{4\alpha N_A Z(Z+1)r_e^2 \log(183Z^{-1/3})} \quad (2.1)$$

where A is the atomic weight and Z is the atomic number of the traversed material, α is the fine structure constant ($\sim 1/137$), N_A is the Avogadro's number ($6.022 \times 10^{23}/\text{mole}$) and r_e is the electron radius ($2.818 \times 10^{-13} \text{ cm}$).

To measure the energy of the incoming particle accurately, the calorimeter must be thick enough in terms of radiation length to contain the electromagnetic shower. To achieve this, a material with high Z and high density is chosen. Lead fulfills this requirement. The ATLAS EM calorimeter has a thickness of at least $22 X_o$.

2.2 Energy deposited in ATLAS EM

Charged particles in the shower lose energy mainly by ionizing the material they traverse. For high-energy particles, the ionization loss rate rises approximately logarithmically with the energy. Electron-Ion pairs created in the liquid argon (active region) are separated by an electric field and drift towards the electrodes inducing an electrical signal that is proportional to the number of created electron/ion pairs and thus to the energy deposited in the liquid argon gap.

In a sampling calorimeter like the ATLAS electromagnetic calorimeter, only a fraction of the total energy is deposited in the active part. The ratio of total energy deposited and energy deposited in the active region is called the sampling fraction:

$$f_{sample} = \frac{E_{Active}}{E_{Passive} + E_{Active}} \quad (2.2)$$

The energy measured in a sampling calorimeter has to be multiplied by the inverse of the sampling fraction and the product is the total deposited energy.

The vast majority of particles in an electromagnetic shower have very little energy and a very short range, typically much smaller than the thickness of the layers. There are only a few tracks that traverse many active and passive layers and thus deposit a certain fraction of their energy in the active region [10]. In contrast, since the muon is a minimum ionizing particle it will indeed pass many layers of the calorimeter, losing a (small) fraction of its energy by ionization and induce only a few secondary particles.

Energy resolution

The number of electrons and positrons in a shower produced by a particle with a given energy fluctuates statistically. Since the total ionization signal is proportional to the number of charged particles the reconstruction energy fluctuates in the same way. The relative width of the distribution is equal to $\sqrt{n}/n = 1/\sqrt{n}$ where n is the number of charged particles. Thus the relative precision of the energy measurement with a calorimeter can be expressed as

$$\frac{\Delta E}{E} = \frac{a}{\sqrt{E}} \quad (2.3)$$

The last equation shows that the relative energy resolution of a calorimeter will be improved with energy. The energy resolution of a calorimeter is usually expressed in terms of a with the Energy given in GeV . There are other effects that contribute to deteriorate the energy resolution of the EMC that can be expressed as:

$$\frac{\Delta E}{E} = \frac{a}{\sqrt{E}} \oplus \frac{b}{E} \oplus c \quad (2.4)$$

The term b takes into account the fluctuation due to noise from the readout electronics and pile-up events. The electronics of the readout system has been designed in order to keep b below 400 MeV. The *constant term* c includes all the effects related to the detector imperfections (active medium impurity, absorbers or gap thickness non-uniformity...) and to the quality of the calibration. For very high energies, the sampling (stochastic) term becomes small and the resolution of the calorimeter is determined by instrumental effects.

2.3 ATLAS Electromagnetic Calorimeter

2.3.1 Electromagnetic Barrel Calorimeter (EMB)

As a sampling calorimeter, the ATLAS EMB calorimeter is built in a way that the shower produced by the incoming particle spreads over many layers of active and passive material. This is done by folding the absorbers and electrodes into an accordion-shape with the folds approximately perpendicular to the incoming particle track. The absorbers are interleaved with electrodes and stacked up, leaving liquid argon filled gaps [11].

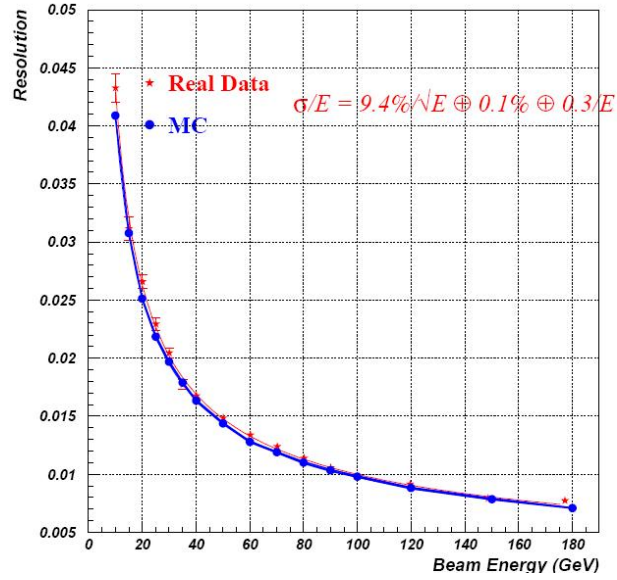


Fig. 2.4: Example of energy resolution [11]

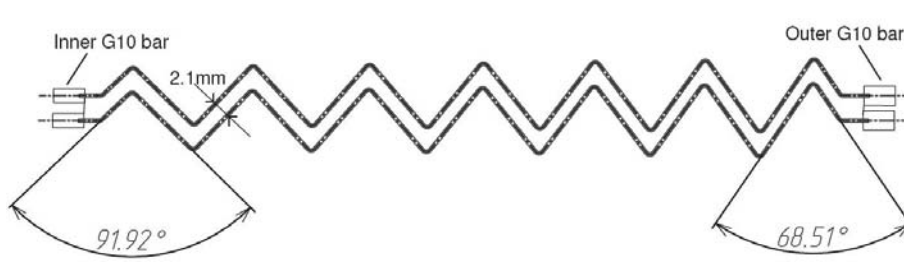


Fig. 2.5: Accordion-shaped absorber with constant gap-size

The accordion folds become bigger and their angle smaller towards bigger radii. This accordion structure allows building of a full wheel with constant gap sizes and hermetically uniform azimuthal coverage. Signal and high-voltage cables are routed at the front and back face of the detector. There are no cables inside the detector volume. The electrodes are held in the middle of the gap by strips of honeycomb spacers laid in the straight section of the accordion (figure 2.5) [7].

The read-out electrodes are placed in the center of the gap between two absorbers (figure 2.6.b). The absorber is made of steel-coated lead and serves as ground electrode. It is 2.16 mm thick; the lead fraction is 1.5 mm thick for $\eta < 0.8$ and 1.1 mm for bigger η . The prepreg layers that glue the steel coats on the lead sheets compensate for the varying thickness. The read-out electrodes consist of three copper layers separated by Kapton layers. The two outer layers carry the high-voltage while the inner one is used as signal layer. It collects the current induced by electrons drifting in the liquid argon gap by capacitive coupling. The liquid argon gap is 2.12 mm wide on each side of the read-out electrode. The two half gaps are supplied by different high-voltage channels to minimize the impact of a high-voltage trip or a short.

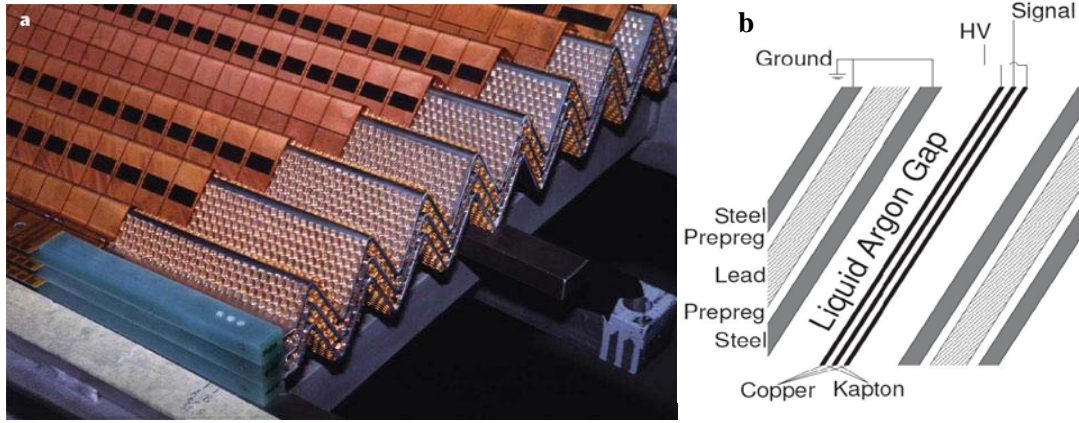


Fig. 2.6: Layers of the electromagnetic calorimeter

Material	Liquid Argon	Lead	Aluminum	Effective values for Accordion ($\eta < 0.8$)
Atomic weight A	39.948	207.2	26.9815386	---
Atomic number Z	18	82	13	---
Density [g/cm^3]	1.381 (at 89.3° K)	11.35	2.66	4.18
Radiation length X_0 [cm]	14.2	0.56	8.9	2.02
dE/dx [MeV/cm] (MIP)	2.1	12.73	4.36	5.3
dE/dx [MeV/ X_0] (MIP)	29.5	7.13	38.8	10.7
Critical Energy (ϵ) [MeV]	38.13	7.79	42.55	---
Molière Radius R_M [cm]	7.79	1.53	11.97	3.66

Table 2.1: lists the properties of the materials used in the construction of the calorimeter [9, 7].

Using the values listed in table (2.1) one can calculate the energy deposit in the active and inactive parts of the accordion and thus the sampling fraction for minimum-ionizing particles (MIP). For the low- η range, a MIP deposits 2.55 MeV in the passive materials (absorber and readout electrode) and 0.89 MeV in the two liquid argon gaps. This yields a sampling fraction of 25%. For the high- η region, the energy deposit in the passive region is only 2.25 MeV due to the lower lead fraction in the absorber. The sampling fraction is therefore 28%. All these numbers are only valid for MIP. Electron showers show a more complex behavior. The exact values for sampling fraction must be obtained from the simulation. The sampling fraction for a shower as

obtained from a Monte-Carlo simulation is smaller than the numbers obtained by the simple calculation. The detail of the sampling fraction simulation of the accordion calorimeter is out of the scope of this study.

The choice of thickness of absorbers and active material is an optimization between sampling fraction (thus the resolution) and total thickness of the calorimeter. For higher η , the total thickness of the calorimeter as seen by a particle coming from the interaction point increases figure 2.7. This is the reason why a thinner absorber is used for higher η .

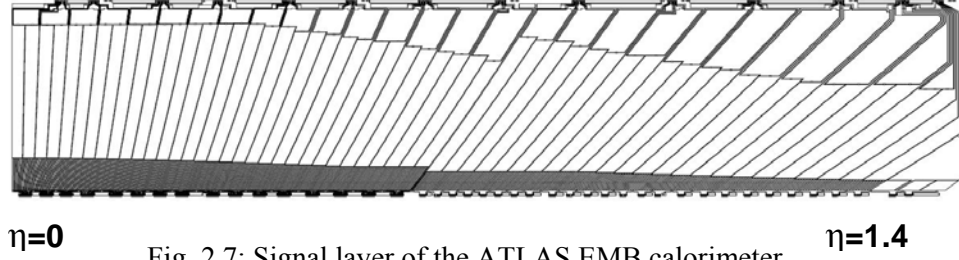


Fig. 2.7: Signal layer of the ATLAS EMB calorimeter.

The barrel calorimeter is subdivided into two identical half-barrels each consisting of 16 modules. Each half barrel is 3.2 m long and contains 1024 absorbers. The inner and outer diameters of the barrel are 2.8 m and 4 m respectively. The EMB contains 150 000 cells. The number of cells is an optimization between achievable position resolution and the readout system complexity. Also noise plays a role, since larger cells pick up more noise. In ϕ , cells are realized by connecting neighboring readout-electrodes together. The segmentation in η and in depth is done by etching the copper of the signal-layer of the electrode like a printed-circuit board (figure 2.7). The cells have 'pointing' orientation i.e, the border lines point to the interaction point. The accordion part is subdivided into three compartments in depth (figure 2.8). The front one has a fine granularity in η (also called 'strips') but is coarse in ϕ . It is between 2.5 and 4.5 X_0 thick. The middle compartment is the thickest one; the bulk of the energy is deposited in it. Each middle cell covers 8 front cells in η but only 1/4 of a front cell in ϕ . The back compartment is even coarser; it serves mostly to catch the end of an electromagnetic shower and to estimate longitudinal leakage. The granularity of the different compartments is summarized in table 2.2.

Compartment	Number of merged gaps	Granularity		Depth in X_0
		$(\Delta\eta \times \Delta\phi)$	w. r. t Middle	
Front	16	0.00375×0.1	$1/8 \times 4$	2.5 - 4.5
Middle	4	0.025×0.025	1×1	16.5 - 19
Back	4	0.050×0.025	2×1	1.4 - 7

Table (2.2) EMB layers Granularity [7]

The angular position, usually defined by the pseudorapidity η and the azimuthal angle ϕ (in radians), is often indicated by the coordinates η_{cell}, ϕ_{cell} , which are expressed in units of Middle layer cells. Therefore, the Middle cell at lowest η, ϕ in the module is labeled

by $\eta_{cell} = 0, \phi_{cell} = 0$ and since the granularity of this layer is $\Delta\eta \times \Delta\phi = 0.025 \times 0.025$, the following general relation holds:

$$\begin{cases} \eta = (\eta_{cell} + 0.5) \times 0.025 \\ \phi = (\phi_{cell} + 0.5) \times 0.025 \end{cases} \quad (2.5)$$

References to middle cells will often have the form Mx , where $x = \eta_{cell}$ runs from 0 to 54 in the EMB (e.g. the first eight cells in electrodes B are named M32 to M39). Each pair of middle cells share the same back cell, therefore referencing will be based on the number of the associated even middle cell (e.g. B32 refers to the back cell shared by M32 and M33).

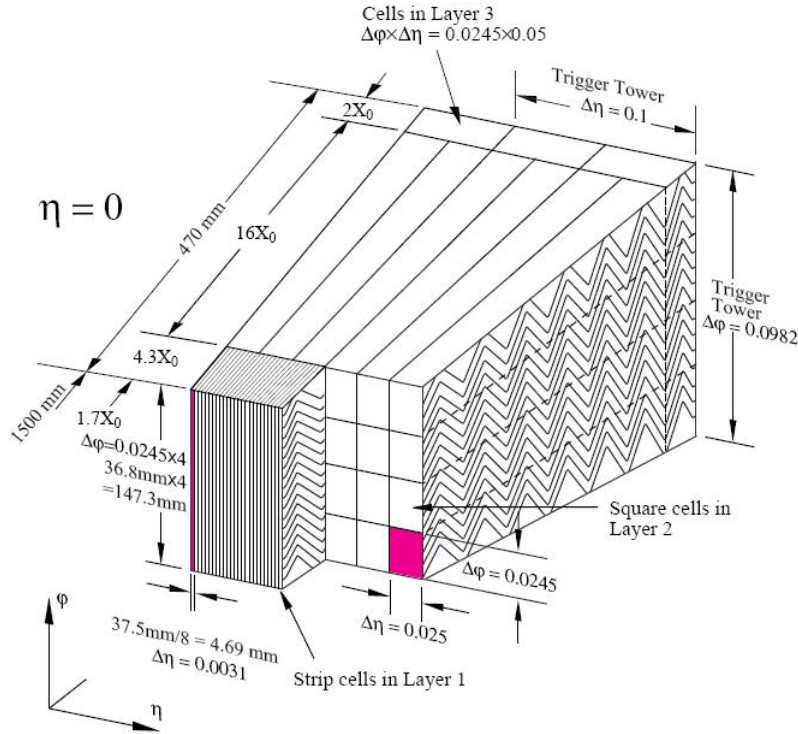


Fig. 2.8: Sketch of a barrel module

2.3.2 Barrel presampler (PS)

The PS is a thin (11 mm) active layer of liquid argon in front of the EMBC. It is used to correct for energy loss upstream of the calorimeter. The PS is subdivided into 32 identical azimuthal sectors per half-barrel, each spanning $\pi/32$ in ϕ . Each sector consists of eight modules, each covering a region of 0.2 in η . Consequently, the modules have unequal length. A PS module is shown in figure 2.9.

The PS modules are made of interleaved cathode and anode electrodes glued between glass-epoxy composite plates. The electrode spacing varies slightly, from 1.9 to 2.0 mm, with the presampler module type. The cathodes are double-sided printed-circuit boards while the anodes

have three conductive layers separated by glass-fiber composite layers. The required segmentation, $\Delta\eta \sim 0.025$ and $\Delta\phi = 0.1$, for each module is obtained by ganging the appropriate number of anodes in the η direction and by etching each anode into two halves in the ϕ -direction. The high-voltage is applied to the outer layers of the anodes and the signal is read out through capacitive coupling to the central layer at ground potential [12].

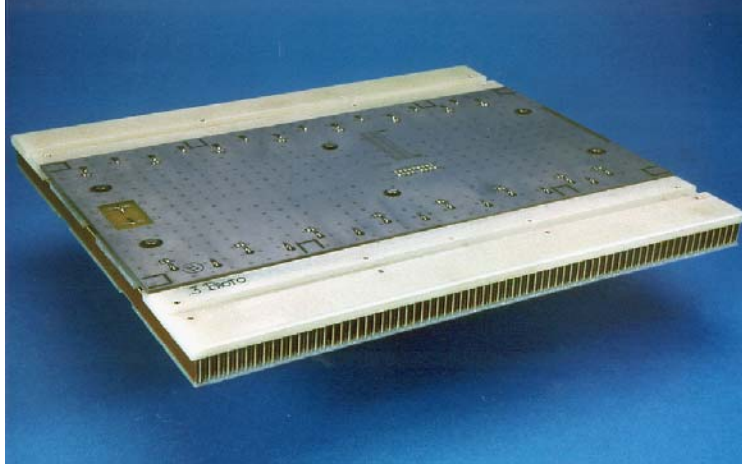


Fig. 2.9: Photograph of a PS module

2.4 Signal processing in ATLAS EM calorimeter

2.4.1 Electronic installations in the cryostat and feedthroughs

The connections from the cells pad to the edge of the electrode are done by etched lines on the copper of the electrode. The front compartment is read out on the inner radius while middle and back compartment on the outer radius. The summing boards are soldered directly on the signal electrodes. They interconnect electrodes belonging to the same readout cell according to the desired ϕ -granularity (see table 2.2). The Motherboards are placed on top of the summing boards and provide readout for cells of a region of $\Delta\eta \times \Delta\phi = 0.2 \times 0.2$. Motherboards distribute also the calibration pulses to the cells using precision resistors. The signal from the motherboards is guided through mini-coaxial cables to patch panels (located at the outer ends of the two half barrels) and to the signal feedthroughs. According to the cable length and capacitance of the detector cells two different cable impedances have been chosen: 25Ω for the middle and the back section and 50Ω for presampler and front cells.

The feedthroughs provide the electrical connections through the cryostat walls with minimal loss of heat. They consist mainly of a cold and a warm flange connected by flexible bellows to allow for the movement coming from thermal contraction of the inner cryostat vessel. The space between the two flanges is pumped down to $\sim 10^{-3} \text{ mbar}$. Flat polyamide strip-line cables connect the warm and the cold flange. Their impedance is 33Ω , a compromise between the 25Ω and the 50Ω cables used inside of the cryostat. There is one feedthrough per module each equipped for 1920 signal lines as well as calibration and monitoring cables.

2.4.2 Front-End electronics

The Front-End electronics is housed in Front-End crates (shown in blue in figure 2.10), that sit directly on the feedthroughs (in red), as close as possible to the cryostat. One Front-end crate covers two feedthroughs. The signal cables end at the backplane of the Front-End crate where the Front-End boards (FEB) are plugged in. To equip one feedthrough, 14 Front-End Boards plus one Monitoring board, one Controller board, one Calibration board and one Tower-builder board are needed.

A schematic view of a typical FEB is shown in figure 2.11. On the FEBs, the signal is amplified, shaped, sampled and digitized. Each FEB can process the signals of up to 128 cells. There are a few FEBs where not all channels are actually connected to calorimeter cells. The first element of the read-out electronics chain is the preamplifier. This is a current sensitive low-noise amplifier. A different preamplifier is used, depending on the cell type (presampler, front, middle or back) to account for the different ionization current and cell-capacitance. Each FEB serves only channels of one kind so they are equipped with the same type of preamplifier. Different FEBs are distinguished according to their preamplifier-type.

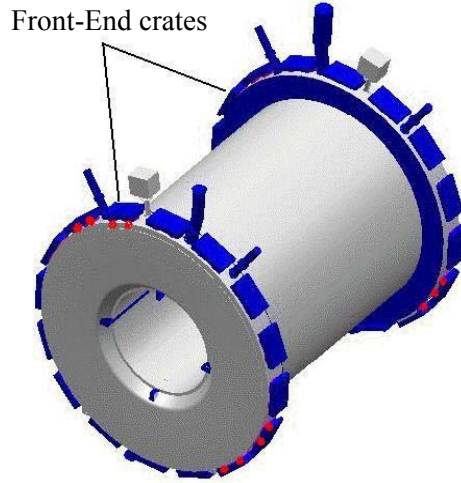


Fig. 2.10: EMB Cryostat

The amplified signal is shaped by a multi-gain $CR-RC^2$ filter [21], whose internal time constant $\tau_{sh} = 15$ ns has been chosen in order to optimize the signal-to-noise ratio. The shaper consists of one differentiator to shorten the tail of the physics signal followed by two integrators to limit the bandwidth and therefore the electronic noise. The physics signal which has triangular shape is transformed into a short peak and a long undershoot (see figure 2.12). The peak amplitude is still proportional to the energy deposited in the cell. In case of pile-up (energy deposited in the same cell by a closely subsequent event) the peak of the second signal can be superimposed on the undershoot of the first signal. For each calorimeter cell, there are three shapers with different gains. The gain ratio is approximately 1:10:100. This extends the dynamic range of the ADC.

The shaped signal is sampled at 40 MHz LHC bunch-crossing frequency (i.e. one sample every 25 ns, figure 2.12) and the values are stored in an analog pipeline (Switched Capacitor Array, SCA) where they wait for the decision from the LVL1 trigger system. There are three

SCAs per cell for the three gains of the shaper. The sampling phase is adjusted in a way that one sample is close to the signal peak. The SCA can hold 144 samples. Given the sampling frequency, the depth of the SCA is $3.6 \mu\text{s}$ that is largely sufficient to cover the maximal latency of the LVL1 trigger (max. $2.4 \mu\text{s}$). The actual latency of a LVL1 trigger-accept is a configuration parameter of the Front-End boards that determines which set of the 144 stored samples is to be digitized.

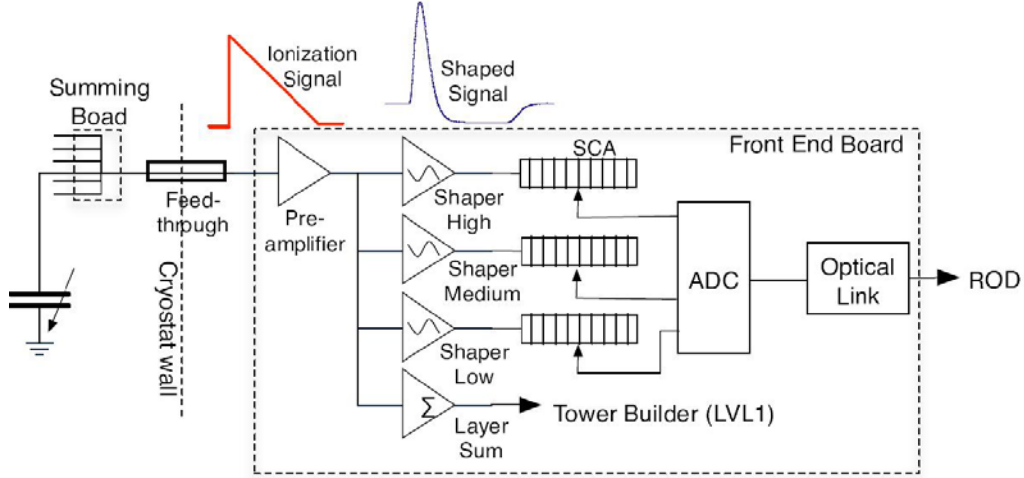


Fig. 2.11: LAr Calorimeter readout chain from the calorimeter cell until digitization.

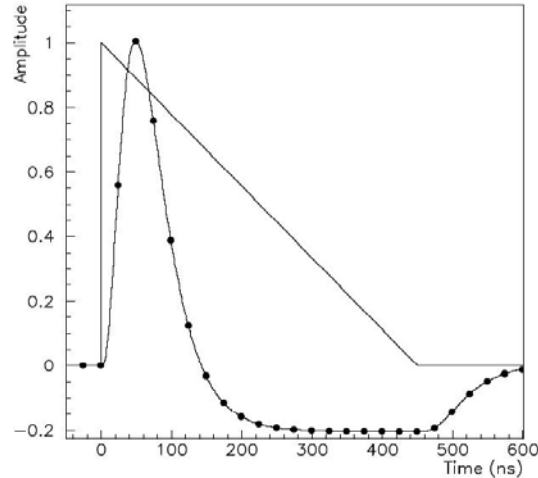


Fig. 2.12: Amplitude versus time for triangular ionization signal and of the FEB output signal after bi-polar shaping (sampling points are shown).

Only if an event is accepted by the LVL1 trigger system, the digitization takes place. The Liquid Argon Calorimeter electronics can cope with a LVL1 trigger frequency of 75 kHz. In data-taking mode, it is planned to read five successive samples, arranged in a way that the maximum is at the second sample. The hardware allows to record up to 32 samples. In automatic gain mode, the gain selection logic uses the second ADC sample to decide which of the three gains will be used. The lower limit for medium gain is approximately 1300 ADC counts, the upper one is approximately 2500. This ensures that no element of the electronics chain saturates. Alternatively, the FEBs can be configured to run in fixed gain mode. The digitized samples of all channels of a FEB are sent over an optical link (GLINK) to the Read-out driver (ROD). The RODs are located in the counting room (see section 2.5), away from the detector. A FEB is

cooled by a 'leak-less' under-pressure water circuit to keep the temperature of the electronics and the surrounding detectors at an acceptable level.

2.5 Calibration system

The task of the calibration system is to measure the response of the electronics chain in-situ to avoid the deterioration of the stability and uniformity of the ionization signal in LAr EM calorimeter by possible degradation of the readout electronics. The calibration board (figure 2.13) injects an exponential pulse with a known amplitude and a shape near to that of the triangle physics pulse and as close as possible to the point where the ionization current is picked up. The calibration pulse is generated by switching the inductance L that is fed by a precision current source. The same pulse is split among several calorimeter cells via a resistive network on the motherboard. The calibration signal is a pulse with a short rise time and an exponential decay (with a decay time τ_{cali}) instead of a linear decay as the ionization signal. The current is set by a digital to analog converter (DAC). The DAC value determines the amplitude of the calibration signal. The pulsers are located on a calibration board in a warm environment but as close as possible to the detector. These boards are installed in the same Front End crates as the FEBs. Only the resistive network to distribute the signal to many calorimeter cells is located inside the cryostat, on the motherboards. The set of cells that is connected to the same calibration line is chosen in a way that cross-talk studies can be carried out, i.e. direct neighbors are not pulsed by the same line. One calibration line pulses 16 presampler cells or 32 front cells or eight middle or back cells. Thus a full barrel module can be calibrated by the 64 pulsers of a single calibration board. The calibration board has a programmable delay chip on the trigger line that can delay the pulse in steps of 1 ns.

The calibration resistors vary depending on the dynamic range of the cells. For the front cells a calibration resistor is 3 k Ω , for back and the middle cells with $\eta < 0.8$ it is 1 k Ω . The middle cells with $\eta > 0.8$ are equipped with 500 Ω resistors.

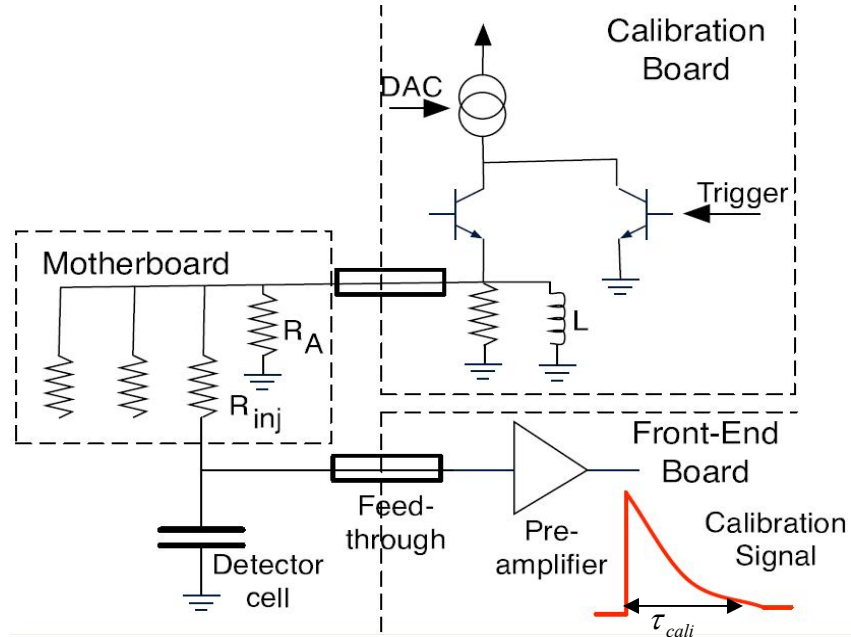


Fig. 2.13: The electronic calibration system.

2.6 Back-end electronics

The back-end electronics [13, 14] located at the counting room (USA15) include the readout driver (ROD) system, which constitutes the core of the backend, the trigger, timing and control (TTC) system, and the LVL1 trigger receiver. The back-end system reads the data from the front-end electronics, and digitally processes the data before transmitting it to the data acquisition system at a L1 trigger rate of up to 75 kHz for the physics data-taking mode and at a 10 kHz rate for the calibration mode. The back-end system also receives the TTC signals, distributes the timing clock and trigger to the front-end electronics and the 192 ROD's, and configures and controls the front-end crates. All of these tasks must be performed fast enough to cope with the above trigger rates.

The ROD task is to receive data from the front-end electronics, to digitally process and format the data and to perform various data-integrity checks and higher-level monitoring tasks. The ROD module comprises a ROD mother-board on which up to four processing-unit (PU) mezzanine cards are mounted. Each processing unit houses two commercial Digital Signal Processor (DSP) chips operating at 720 MHz . Each DSP is preceded by an input buffer used to perform data-integrity checks as well as to reformat the input data to suit the DSP architecture. Following each DSP is an output buffer used to buffer processed events before transfer to the data acquisition system. For each trigger, data from the TTC stream and from the front-end electronics are pushed into the ROD modules, where they are checked, processed, formatted and sent on a readout link to the ATLAS data acquisition system.

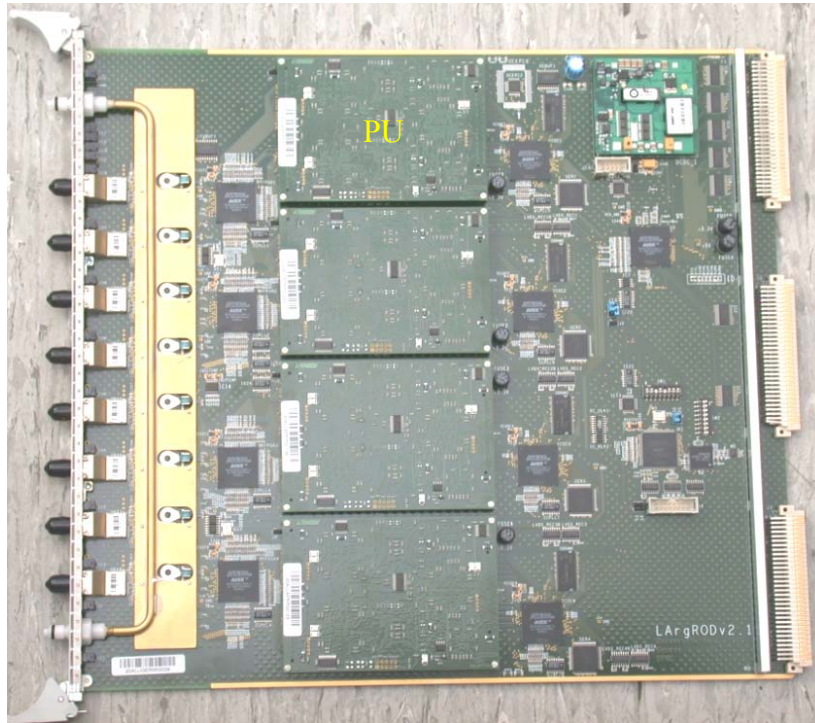


Fig. 2.14: The Readout derive (ROD)

In physics mode, the output contains the roughly calibrated cell energy in MeV. This is mandatory to allow the second level trigger a fast evaluation of the energy deposit in the calorimeter. The DSP can also forward the raw data unchanged to the output. This mode ('transparent mode') is used e.g. for detector tests.

Chapter 3

Energy reconstruction of a single cell

3.1 Main principle

The ADC samples of the shaped physics pulse are sent from the FEB to the ROD via an optical link (GLINK). These ADC samples are the basis for the energy calculation together with calibration data acquired during calibration runs. The ADC has a pedestal of roughly 1000 counts to accommodate the undershoot of the shaper. This pedestal has to be subtracted from the samples. The next step is to compute the peak of the physics pulse (see figure 2.12). The standard method that has been chosen by the Liquid Argon group is the optimal filtering method (section 3.3.1). Alternatively, the peak can be found by fitting second or third order polynomials to the samples. Once the amplitude of the signal is known, one has to apply the ADC to energy conversion factor. This includes the electronic gain, the current-to-energy conversion factor as well as the sampling fraction of the calorimeter. The electronic gain can also be a higher order polynomial to take small non-linearities into account [15]. This first step of the energy reconstruction is done by the DSP located on the ROD.

Only in special cases like during commissioning, for special triggers or for cross-checks the raw ADC samples are written out (transparent mode). By default, only the energy of each cell is sent to the byte stream. This is necessary in order to allow the trigger system to evaluate the energy of a region of the calorimeter in the given time budget. For further physics analysis, a more refined offline-calibration is done.

3.2 Offline software implementation

The software package LArROD contains the Athena algorithms required to calculate the energy of a single cell. This name was chosen because it mimics the functionality of the hardware ROD. These algorithms take a LArDigitContainer (usually read from the byte stream file) and produce a LArRawChannelContainer using various kinds of calibration data that come from the conditions database. There are two algorithms available to do the step from raw ADC counts to energies.

- The LArRawChannelBuilderDriver that is closely related to the LArRawChannelBuilder algorithm which uses the method of Optimal Filtering. The driver itself is used to loop over the LArDigitContainer. The creation of LArRawChannel is performed in three steps: (1) subtract the pedestal, (2) finding the peak, and (3) convert ADC counts to energy in MeV.
- The LArRawChannelSimpleBuilder provides an alternative computation of energy if the optimal filtering coefficients or other calibration constants are not available. It is mainly intended for monitoring in a beam test environment, when no complete calibration is available.

3.3 Ionization signal reconstruction

3.3.1 The Optimal Filtering method

Optimal Filtering (OF) [16] is a digital filtering technique that is used to reconstruct the peak A of a shaped ionization signal and the arrival time τ as a linear combination of the pedestal subtracted samples s_i

$$A = \sum_{i=1}^N a_i (s_i - p) \quad (3.1)$$

$$A\tau = \sum_{i=1}^N b_i (s_i - p) \quad (3.2)$$

where a_i and b_i are the Optimal Filtering coefficients (OFC), s_i are ADC samples and p is the pedestal. Equations 3.1 and 3.2 are applied by the Digital Signal Processors (DSP) which is on the ROD boards. The linear structure of equations (3.1), (3.2) allows a fast computation of the amplitude and the time of the pulse. The OFCs are computed through a Lagrange multipliers procedure that aims to minimize the noise contribution, both from electronics and pile-up contributions. The LArRawChannelBuilder can only reconstruct the arrival time τ if the ADC peak is above a certain threshold (sufficiently high above noise) which is set by the so-called job-options.

The OFCs are calculated from the following formula for the signal

$$S(t) = A \cdot (g(t) - \tau \cdot g'(t) + n(t)) \quad (3.3)$$

where $g(t)$ is the normalized shaped ionization signal and $g'(t)$ is its first derivative; $n(t)$ is the noise component given by the noise autocorrelation matrix. Because these quantities differ from one cell to another, one set of OFCs per cell and per shaper gain is needed.

One can also compute the quality factor Q by comparing the measured pulse shape with that of the reference shape:

$$Q^2 = \sum_{i=0}^n (s_i - A \cdot (g_i - g'_i))^2 \quad (3.4)$$

The quality factor Q makes only sense if there is enough signal above noise, like in the case of arrival time.

3.3.2 Alternative methods to compute the ADC peak

The OF technique is not the only method to reconstruct the ADC peak, the algorithm LArRawChannelSimpleBuilder provides also the following procedures that had been used during test beams:

Highest Sample; selects the highest ADC sample. This can lead to a positive bias since the noise is not subtracted.

Fixed Sample; selects a sample which has an index that is defined in the job option.

Cubic Interpolation; interpolates a third order polynomial on 4 samples. This method is only applied if the signal is above a certain threshold (typically 15 to 20 ADC counts).

Parabola Fit; interpolates a quadratic polynomial on the 3 highest samples. In this method a phase-dependent correction can be applied. As in the case of Cubic Interpolation, it is only used if the signal is above a certain threshold. This method leads to the second-best results after Optimal Filtering.

3.4 The signal peak to energy conversion factor

The factor which converts the signal peak (measured in ADC counts) to cell energy in MeV is the product of many sub-factors:

- Ramp factors which express electronic gain
- The $F_{DAC \rightarrow \mu A}$ factor.
- Current-to-energy conversion factors
- Charge-Collection correction (Cross talk)

3.4.1 The Ramp factors

The relation of ADC counts to ionization current is measured on a regular basis by the electronic calibration system. The output of calibration procedure is a fit of DAC values to ADC values. The ADC to DAC fit can be either linear or polynomial to take possible non-linearities of the electronic chain into account. The DAC has 16 bit resolution and is fed with 5 V. The ratio of DAC setting to injected current is given by

$$\frac{I_{inj}}{DAC} = \frac{5V}{(2^{16} - 1)R_{inj}} \quad (3.5)$$

where R_{inj} is the injection resistor on the motherboard.

The energy calculation which is done in the ROD uses only a ramp obtained by refined straight line fit because such a calibration can be easily undone offline to apply a more refined calibration. The LArRawChannelBuilder uses a ramp that is a higher-order polynomial. Whether the intercept of the fit is used or not depends on the job option settings. Analysis of 2004 test beam data suggests that using the intercept in medium gain improves the linearity [17].

The LArRawChannelSimpleBuilder can use a hard-coded ramp as fall-back solution in case the electronic calibration is not available. There is one such number per gain and per layer of the calorimeter except of the middle layer where two numbers per gain are necessary to take the changing of the absorber thickness at $\eta = 0.8$ into account.

3.4.2 The $F_{DAC \rightarrow \mu A}$ factor

This factor is given by the calibration board parameters and the injection resistor on the motherboard

$$F_{DAC \rightarrow \mu A}(\mu A / DAC) = \frac{76.295 \mu V}{R_{inj}}, \quad (3.6)$$

where R_{inj} is the injection resistor.

3.4.3 Current-to-energy conversion factors

In the straight sections of the accordion folds, the electric field is homogeneous. In this case, the factor which converts the deposited energy to the induced current can be easily calculated from the drift time and the average energy needed to create a single electron/ion pair. For Liquid Argon, this corresponds to $W = 23.6$ eV per e^- / ion-pair [7]. Since ions drift very slowly inducing a small current, the ion current can be neglected in the following calculation. In contrast, electrons drift quickly and induce a current at the signal electrode. As the electrons get absorbed by the anode, the current decreases. This explains the triangular shape of the physics pulse (see figure 3.1).

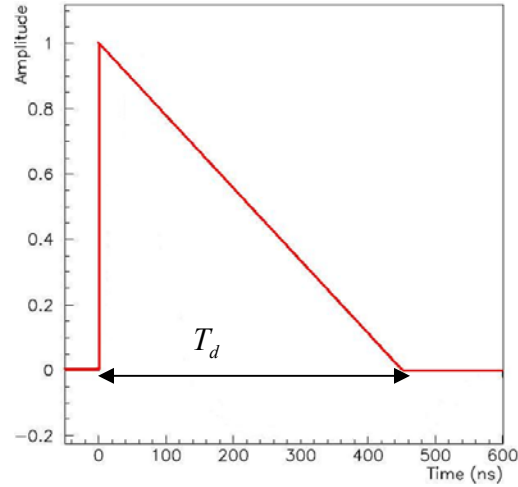


Fig. 3.1: Signal induced by the drift electrons in LAr

The peak current per deposited charge q is given by:

$$I = \frac{q \cdot v}{d} \quad (3.7)$$

Since the drift time is determined by the gap width and the electron velocity v ($T_d = d / v$) and the charge induced by 1 eV is given by $q/E = e/W$, equation 3.6 can be written as

$$I/E = \frac{e}{W} \cdot T_d \quad (3.8)$$

The drift velocity v depends on the electric field and on the temperature of the liquid Argon (LAr). In a very high electric field the velocity is no longer proportional to the field strength. The electron drift velocity in argon in the relevant temperature and electric field range had been studied and an empirical formula was given [18]. Assuming a constant temperature, the drift velocity is roughly proportional to $E^{0.3}$.

As seen in section 2.2, the sampling fraction f_{sample} (or F_{PS} for the PS) can be computed using Monte Carlo simulation.

Compartment	I/E ($\mu A/MeV$)	f_{sample} (or F_{PS})	$F_{\mu A \rightarrow MeV} = 1/(I/E \times f_{sample})$ ($MeV/\mu A$)
PS $\eta < 0.8$	0.0174	0.05	1149
PS $\eta > 0.8$	0.0174	0.05	1149
Accordion $\eta < 0.8$	0.016	0.1667	375
Accordion $\eta > 0.8$	0.016	0.1959	320

Table 3.1: I/E and f_{sample} (or F_{PS}) values for PS and Accordion

Table 3.1 shows typical values for I/E and f_{sample} (or F_{PS}) values for PS and Accordion. These numbers are only valid for the straight section of the accordion, where the electric field is homogeneous and recombination is neglected.

Alternatively, the I/E factor can be derived by comparing the energy deposit predicted by the Monte-Carlo simulation with the current measured in the beam test, assuming that all other effects are properly described in the simulation. Such a comparison was carried out with beam test data from 2002 (where the beam energy was precisely known) and yielded a value of 16 nA/MeV [15].

3.4.4 Cross talk

The readout signal of the calorimeter cells is mostly affected by capacitive cross-talk. Detailed measurements have been performed during previous beam tests [19] and a cross talk map (see figure 3.2) has been produced. The biggest cross-talk can be observed between neighboring strip cells, the strip-strip peak to peak capacitive cross-talk is about 7.17 % and 0.81 % for 1st neighbor strip and 2nd neighbor strip respectively [29].

Cross-talk has two major effects on the readout signal: first, a fraction of the energy of a cell is spread out to its neighbors and second, the pulse shape is distorted. Since neighboring cells will be most likely contained in the same cluster, the loss of signal to the neighbors does not change the cluster energy significantly during physics run. But in calibration runs, every cell is pulsed individually independently from its neighbors so signal gets lost to the neighbors and the reconstructed calibration pulse peak is lower. This effect is relevant in the strips and has to be corrected.

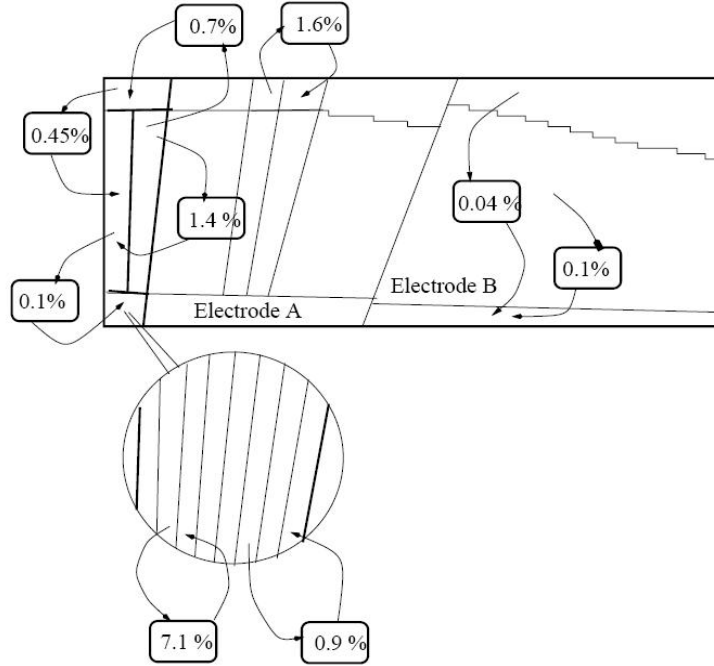


Fig. 3.2: Cross-talk measured in module M13 [19].

3.5 Electronics calibration

3.5.1 Calibration constants

The calibration constants depend on the properties of the electronic readout chain and may vary with time. These constants are obtained through dedicated calibration runs using the electronic calibration system (see section 2.4). In general, the calibration constants vary from cell to cell and different for each of the three gains. Therefore they have to be measured individually for each cell and each gain. To avoid the effect of cross-talk, or possibly to measure it, neighboring cells are not pulsed at the same time.

3.5.2 Pedestal runs

The pedestal corresponds to the ADC counts of a channel without any energy deposit. It takes about 1000 ADC counts to accommodate the undershoot of the shaper. The pedestal signal depends slightly on the temperature of the FEB. During data taking, it is planned to measure the pedestal every 8 hours. This is what had been done during the beam test 2004 [15]. One pedestal run consists of about 2000 events for each gain. The pedestal used in the reconstruction (equations 3.1 and 3.2) is obtained by averaging over all events and all ADC samples for each channel and each gain. Also, the electronic noise and the noise autocorrelation matrix can be calculated. The noise autocorrelation is an input parameter for the Optimal Filtering computation and the noise level is used for clustering.

Moreover, pedestals can also be calculated on random events (events in which the readout is triggered independently of the particles that traverse the detector), if they are available.

3.5.3 Ramp runs

The electronic gain gives the relation between the ionization current and ADC counts. The calibration system allows sending well-defined pulses of different amplitudes through the electronics chain. The amplitude of the calibration pulse is given by the input to the DAC (Digital-Analog converter) and by the precise calibration resistors. Thus the current to ADC calibration can be measured in-situ at any time. In Ramp runs, the cells of the calorimeter are pulsed with increasing DAC values. For each point, about 100 events are recorded. Similar to the pedestal runs, such measurements will be carried out every 8 hours. Figure 3.3 shows an example of a ramp in a middle cell. Experience of the test beam shows that the gain changes by about 1% per 4° change in FEB temperature [17].

The calibration signal amplitude, which is needed to analyze a ramp run, is calculated using the calibration OFCs. The actual ramp is now the correlation between the pulse peak in ADC counts and the input DAC value that corresponds to an electrical current. It could be fitted either to a straight line or to a higher-order polynomial function as done during test-beams. In ATLAS a straight line fit is used.

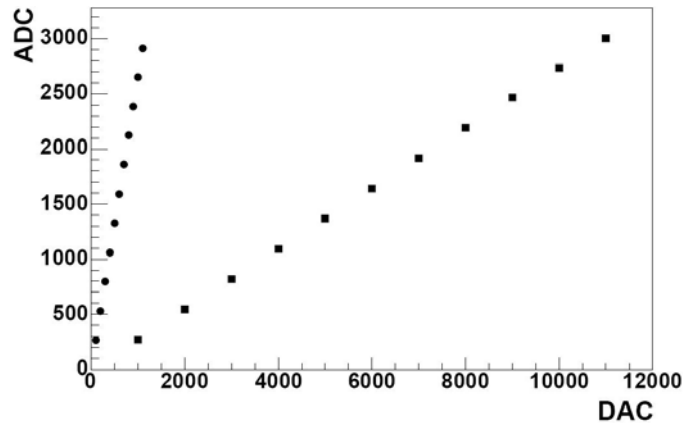


Fig. 3.3: Example for ramps in high gain (circles) and medium gain (squares) in a cell of the middle compartment.

3.5.4 Delay runs

A delay run aims to acquire the signal shape which is necessary to calculate OFCs. In delay runs the channels are pulsed by the calibration system and delaying the readout in steps of about 1 ns. Since the ADC samples are accommodated in 25 ns intervals, 25 delay steps are necessary to cover the whole signal shape. The number of acquired ADC samples defines the fraction of the shape that is sampled. If only 5 ADC samples are recorded (as in the case of physics data), only the first 125 ns are covered. That is the fraction of the pulse that is used for physics runs. To record the exponential tail of the signal, longer delay runs are necessary. The Front-End electronics allows for runs up to 32 samples (800 ns).

The ionization signal differs from the calibration one for two reasons. Firstly the current produced by drifting electrons is triangular, with a duration equal to the drift time T_d (figure 3.1), whereas the injected calibration current is exponential, with a decay time τ_{cali} (section 2.4). Secondly the former is generated inside the detector, while the latter is injected on the signal collection board, at one end of the detector, and reaches inside the detector through an inductive path. The differences can be corrected mathematically using the electrical properties of the readout chain [20], or by fitting the physics pulse profile to a calibration pulse profile. Figure 3.4 shows an example of a calibration signal shape and the corresponding predicted physics pulse shape.

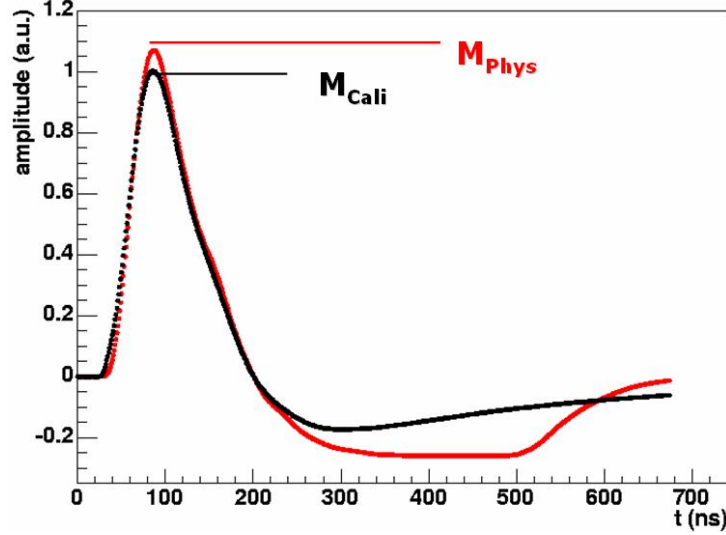


Fig. 3.4: Example for a shaped calibration pulse (black) and the corresponding predicted physics pulse shape (red).

The peak difference between the shaped calibration and the shaped physics pulse is a result of the different injection points and the difference of the shapes of the two injected current signals. The factor between physics and calibration pulse height is known as M_{phys}/M_{cali} factor. Since the ramp is taken on a calibration pulse, it is systematically wrong by this factor and has to be corrected.

3.6 Energy reconstruction of a single cell

From the above discussion, the energy content of a single cell can be given by;

$$E_{Cell} = F_{\mu A \rightarrow MeV} \cdot F_{DAC \rightarrow \mu A} \cdot \frac{1}{M_{phys}/M_{cali}} \sum_{i=1}^{M_{ramps}} R_i \left[\sum_{j=1}^{N_{samples}} a_j (s_j - p) \right]^i \quad (3.9)$$

where p is the pedestal, a_j are the OF coefficients, R_i is the electronic gain (ramp), described by a M_{ramps} order polynomial, M_{phys}/M_{cali} is the factor that accounting for the difference between the amplitudes of a calibration and an ionization signal of the same current, $F_{DAC \rightarrow \mu A}$ is DAC to

current conversion factor which depends on R_{inj} and $F_{\mu A \rightarrow MeV}$ is the current to energy conversion factor.

As already shown in section 3.3.1 the OF coefficients are computed using a Lagrange multipliers procedure whose goal is to minimize the noise contribution, both from electronics and pile-up contributions. The later has zero average and can be treated as a noise source due to the use of bipolar shaper. This method assumes that both the noise autocorrelation function and the normalized ionization pulse shape are known. While the former can be directly estimated from random triggering data or pedestal runs, the latter cannot be easily measured at ATLAS, but needs to be predicted from calibration pulse shapes. The physics pulse prediction will be the subject of chapter 4.

3.7 Signal description

At the end of this chapter the mathematical description of both the physics and the calibration signals are described in some detail.

3.7.1 Physics signal

As already shown in subsection 2.4.2, the ionization electrons drift in the field produced in the LAr gap by the high voltage, producing a triangular shape current signal with amplitude proportional to the released energy and a rise time of the order of 1 ns followed by a linear decay for the duration of the maximum drift time T_d [25]. In the time domain the ionization signal is given by:

$$I_{inj}^{phys}(t) = I_o^{phys} \left(1 - \frac{t}{T_d} \right) \theta(t) \theta(T_d - t) \quad (3.10)$$

and in Laplace domain it will be:

$$I_{inj}^{phys}(t) = I_o^{phys} \left(\frac{1}{s} - \frac{1 - e^{-sT_d}}{s^2 T_d} \right) \quad (3.11)$$

where I_o^{phys} is the current extrapolated to $t = 0$ and $s = \sigma + i\omega$ is the complex frequency. In the complex frequency, the imaginary component $\omega = 2\pi f$, corresponds to the usual concept of frequency, whereas the real component σ of the complex frequency corresponds to the degree of damping (decay rate).

3.7.2 Calibration signal

The calibration signal aims to mimic the ionization signal. It is injected as near as possible to the LAr gap, in order to be able to measure the actual gain and properties of each channel thus assuring the proper cell equalization [7]. The calibration board (CB) that was summarized in section 2.4 can be simplified to the model shown in figure (3.5). It generates an exponential signal with decay time τ_{cali} .

In Laplace domain the calibration pulse is given by:

$$I_{inj}^{cali}(s) = I_o^{cali} \left[\frac{\left(\frac{r_c}{r_c + R_c/2} \right) + s \left(\frac{L_c}{r_c + R_c/2} \right)}{s \left(1 + s \left(\frac{L_c}{r_c + R_c/2} \right) \right)} \right] \quad (3.12)$$

where I_o^{cali} is the height of the inserted step current that flows through the parallel combination of an inductance L_c and a resistance R_c equal to the calibration line termination on the MB. The values of the R_c and L_c components are chosen in order to obtain the proper exponential decay constant $\tau_{cali} = \frac{2L_c}{r_c + R_c}$, which has been chosen to mimic the ionization signal decay slope. The exponential voltage pulse is then converted to a current signal by the calibration resistor located on the MB.

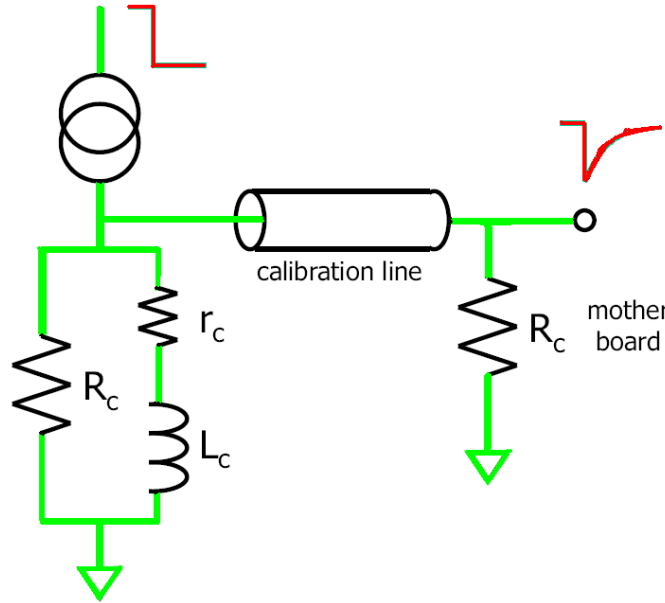


Fig. 3.5: The calibration board pulser circuit.

The ratio $f_{step} = \frac{r_c}{r_c + R_c/2} \in [0,1]$, is the fraction of the resistive component r_c of the non-ideal inductance L_c to the total resistance $(r_c + R_c/2)$. Equation (3.12) then can be written as:

$$I_{inj}^{cali}(s) = I_o^{cali} \left[\frac{f_{step} + s \tau_{cali}}{s(1 + s \tau_{cali})} \right] = I_o^{cali} \left[\frac{(1 - f_{step}) \tau_{cali}}{1 + s \tau_{cali}} + \frac{f_{step}}{s} \right] \quad (3.13)$$

In the time domain the calibration signal is given by:

$$I_{inj}^{cali}(s) = I_o^{cali} \left[(1 - f_{step}) e^{-t/\tau_{cali}} + f_{step} \right] \theta(t) \quad (3.14)$$

Thus the effective calibration pulse is an exponential waveform that converges to a non-zero baseline. The relative height of this residual baseline is determined by the resistive component r_c of the non-ideal inductance L_c of the CB pulser circuit. The nominal value of the resistance on the CB is $R_c = 50$ [26]. An $r_c \sim 2 \text{ } \Omega$ resistive component of the non-ideal inductance L_c can be expected [27], leading to a baseline fraction $f_{step} \sim 7 \text{ } \%$.

Chapter 4

Electrical Properties of the EMC

4.1 Introduction.

It is obvious that the electrical properties of the detector itself have their impact on the uniformity of the energy response of the detector. In this sense, a basic electrical model that describes each detector channel as an LC circuit is inadequate, and we must consider also the effect of the capacitive cross-talk between adjacent detector channels, particularly in case of calibration pulse.

4.2 Basic detector electrical model

The simplest model for a detector cell is shown in figure 4.1. It considers the Liquid Argon (LAr) gap as a capacitor C between the absorber (ground reference) and the readout electrode. The signal originated by an electromagnetic shower (known as "ionization" or "physics" signal) is represented by a triangular current generator applied between the two capacitor plates, I_{inj}^{phys} . This signal is brought to the summing board (SB) and the mother board (MB) through an inductive path which has a total inductance L and a total resistance r (total means that the signal path on the electrode plus the SB and MB contribution). The calibration pulse, I_{inj}^{cali} , is an exponential current generator injected on the MB with a decay time $\tau_{cali} \approx 350ns$.

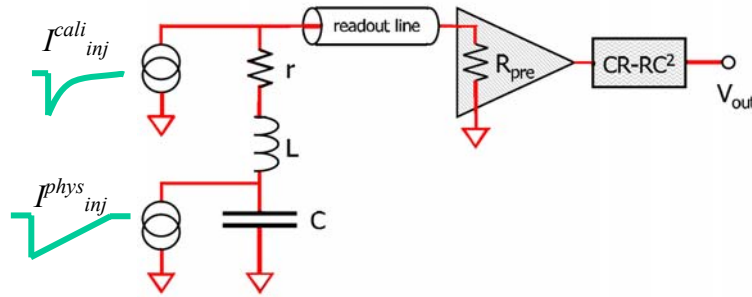


Fig. 4.1: Basic equivalent circuit of the LAr detector readout cell.

The readout line consists of a set of cables connected to each other and closed on a preamplifier with input impedance Z_{PA} is equal to $25\ \Omega$ for middle and back cells and $50\ \Omega$ for front cells (strips), followed by a CR-RC² bipolar shaping filter with time constant $\tau_{sh} = 15ns$ [21]. Then, the transfer function of the readout system is given by:

$$H^{readout}(s) = H_{line}^{readout}(s) \alpha \frac{s \tau_{sh}}{(1 + s \tau_{sh})^3}, \quad (4.1)$$

where $H^{readout}(s)$ is the transfer function of the readout line chain, α is the preamplifier gain, which is considered to be frequency independent, at least within the window of the shaper, and $s = \sigma + i\omega$ is the complex frequency. For typical shaped calibration and ionization signals see figure 3.4.

4.2.1 Ionization signal prediction

In Laplace domain the ionization signal out of the shaper $I^{phys}(s)$ can be predicted from the corresponding calibration one $I^{cali}(s)$ by [28];

$$I^{phys}(s) = I^{cali}(s) \times \underbrace{\frac{(1 + s\tau_{cali})(sT_d - 1 + e^{-sT_d})}{sT_d(f_{step} + s\tau_{cali})}}_{g^{\exp \rightarrow tri}(s)} \times \underbrace{\frac{1}{1 + s\tau_r + s^2\tau_o^2}}_{g^{MB \rightarrow det}(s)} \quad (4.2)$$

where $\tau_r = rC$, $\tau_o = \frac{1}{\omega_o} = \sqrt{LC}$, τ_{cali} and f_{step} are calibration board parameters that depend on the calibration board elements, and T_d is the electrons maximum drift time in the LAr gap.

In time domain equation (4.2) becomes;

$$I^{phys}(t) = I^{cali}(t) \times \underbrace{L^{-1}\left\{\frac{I_{inj}^{phys}(s)}{I_{inj}^{cali}(s)}\right\}}_{g^{\exp \rightarrow tri}(t)} \times \underbrace{L^{-1}\left\{\frac{1}{1 + s\tau_r + s^2\tau_o^2}\right\}}_{g^{MB \rightarrow det}(t)} \quad (4.3)$$

where:

$$g^{\exp \rightarrow tri}(t) = \delta(t) + \left[\frac{(1 - f_{step})}{\tau_{cali}} e^{-f_{step}t/\tau_{cali}} - \frac{(1 - f_{step} - e^{f_{step}t/\tau_{cali}})}{f_{step}T_d} e^{-f_{step}t/\tau_{cali}} \right] \theta(t) + \frac{1}{f_{step}T_d} \left[1 - e^{-f_{step}(t-T_d)/\tau_{cali}} (1 - f_{step}) \right] \theta(t - T_d) \quad (4.4)$$

$$g^{MB \rightarrow det}(t) = \frac{2}{\tau_a} e^{-\tau_r t / 2\tau_o^2} \sin\left(\frac{\tau_a}{2\tau_o^2} t\right) \theta(t) \quad \left(\tau_a = \sqrt{4\tau_o^2 - \tau_r^2}\right) \quad (4.5)$$

The drift time T_d affects the prediction of the ionization signal and its value, which depends on the LAr gap width, the mobility of the electrons in LAr and the applied high voltage, can be estimated by comparing the predicted shape with one observed from electron data ($T_d \approx 470$). The extraction cell electrical properties τ_r and $\tau_o = 1/\omega_o$ that vary from cell to cell and the calibration pulse parameters f_{step} and τ_{cali} that depend on the calibration channel characteristics had already been described in [28]. The next section focuses on the extraction of $\tau_o = 1/\omega_o$ in more details.

4.2.2 Extraction of τ_o from the calibration pulse analysis.

In [28] a set of algorithms is proposed to extract the parameters f_{step} , τ_{cali} , τ_r and τ_o by analyzing only the calibration pulse. The advantage of this technique is that the detector calibration does not rely on the acquisition of ionization signal events and therefore it is completely autonomous process. In Laplace domain the calibration pulse at the end of the shaper is given by:

$$I^{cali}(s) = \underbrace{\frac{f_{step} + s\tau_{cali}}{s(1 + s\tau_{cali})}}_{I_{inj}^{cali}(s)} \times \underbrace{\frac{1 + s\tau_r + s^2\tau_o^2}{1 + s(\tau_r + \tau_Z) + s^2\tau_o^2}}_{H_{det}(s)} \times H_{line}^{readout}(s) \times \underbrace{\alpha \frac{s\tau_{sh}}{(1 + s\tau_{sh})^3}}_{H_{pre+sh}(s)} \quad (4.6)$$

where $\tau_{sh} = 15ns$ is the CR-RC² bipolar shaper time constant, α is the preamplifier gain, $H_{line}^{readout}(s)$ is the transfer function of the readout line and $\tau_Z = CZ_{line}^{readout}(s)$ where $Z_{line}^{readout}(s)$ is the input resistance of the readout line as seen from the detector. The modulus of the detector transfer function is given by:

$$|H_{det}(s)| = |H_{det}(j\omega)| = \frac{\sqrt{(1 - \omega^2\tau_o^2)^2 + \omega^2\tau_r^2}}{\sqrt{(1 - \omega^2\tau_o^2)^2 + \omega^2(\tau_r + \tau_Z)^2}} \quad (4.7)$$

$|H_{det}(s)|$ has a minimum at $\omega_o = 1/\tau_o = 1/\sqrt{LC}$. Following the strategy of the Response Transformation Method, RTM [28]; ω_o value is extracted by finding the minimum of the function:

$$Q^2(\omega) = \sum_{t > t_{tail}} X_{out}^2(t; \omega) \quad (4.8)$$

where $X_{out}(s; \omega) = C_{inj} \times H_{det}(s) \times H_{readout}(s)$ is the response of the system to a monochromatic cosine pulse $C_{inj}(t; \omega) = \theta(t)\cos(\omega t)$ of angular frequency ω . Although extracting ω_o as discussed above works fine for about one-half of the readout channels, the situation in strips is not so easy because usually there is more than one minimum, see figure 4.2.

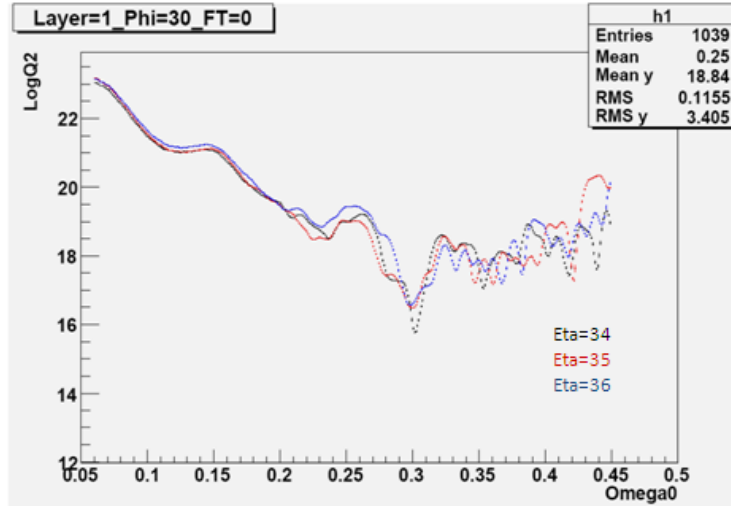


Fig. 4.2: Frequency response for a typical calibration signal for front compartments (ω_o in GHz).

The function shown in figure 4.2, looks smoother if the integration is taken around the pulse peak range (shown in blue in figure 4.3) instead of tail range (shown in red in figure 4.3). This is due to that the tail region is affected by cable effects more than the peak region.

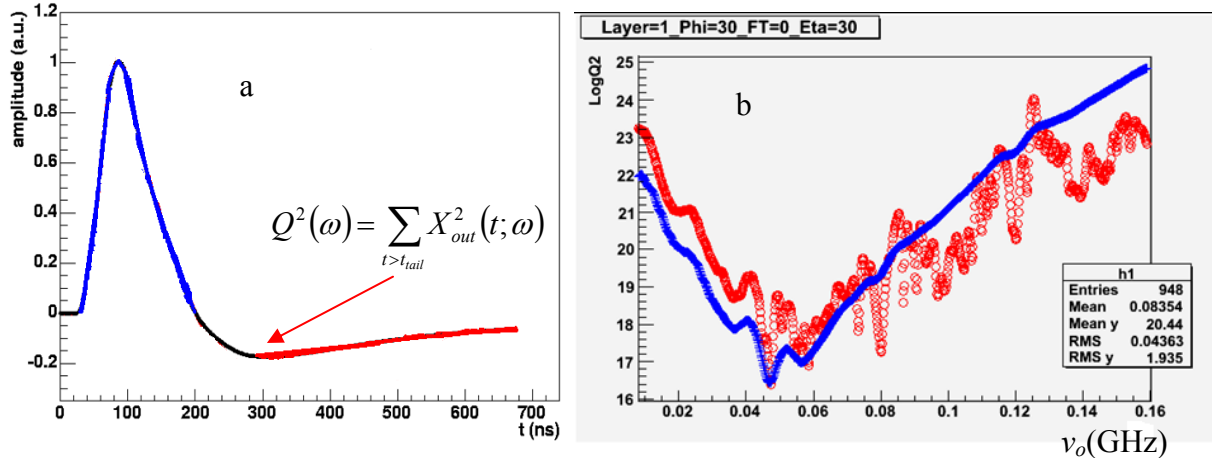


Fig.4.3: (a) a typical calibration pulse, (b) frequency response for the calibration signal from front layer, ($\nu_o = \omega_o/2\pi$).

4.3 A circuit simulator as electrical detector model

Using the SIMetrix circuit simulation package, one can explore the electrical properties of the LAr detector. Figure 4.4-a shows the drawing of a cell simulation without taking effects from adding cables, such as reflections into account.

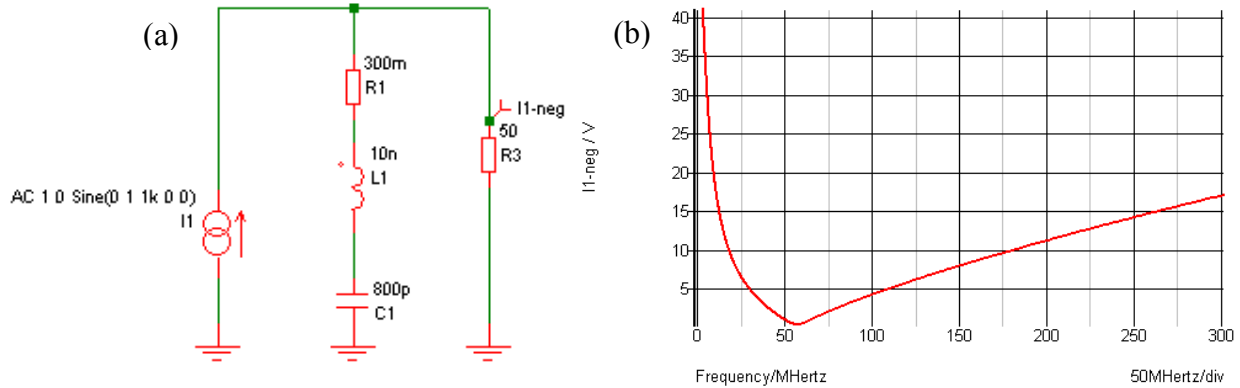


Fig. 4.4: (a) Schematic of a cell, (b) rLC resonance curve.

In figure 4.4-a, R_1 (the damping resistance), L_1 and C_1 represent the detector cell. R_3 represents the preamplifier input impedance which is considered to be a flat resistor for simplicity. The injected calibration signal is generated by an ideal current source. As shown in figure 4.4-b, the output signal corresponds to the resonance curve for an rLC circuit with a frequency $\nu = 56.269$ MHz which corresponds to $\omega_o = 1/\sqrt{L_1 C_1} = 35.355 \times 10^7$ rad/sec.

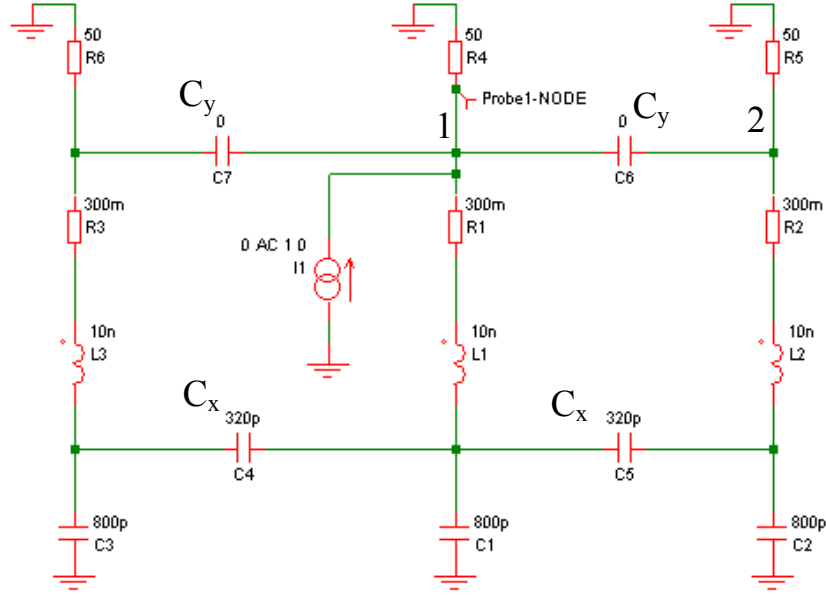


Fig. 4.5: Schematic of a cell with a capacitive cross talk with just two neighboring cells one on each side.

4.3.1 Capacitive cross-talk effects

To study the effect of neighboring cells, the circuit shown in figure 4.5, is considered. The pulsed cell is represented by R_1 , L_1 and C_1 and its output is taken through the preamplifier R_4 , while the neighbors are represented by R_2 , L_2 , and C_2 , and R_3 , L_3 , and C_3 . The capacitive cross-talk can be subdivided into two contributions;

1. The coupling on the level of the detector cells (the LAr gap) which is represented by the capacitors C_4 and C_5 which is called C_x for simplicity.
2. The coupling on the level the readout chain (on the level of the SB) which is represented by the capacitors C_6 and C_7 which is called C_y for simplicity.

Now, one can select different values for capacitive cross talk and see the response of our network. The impact of cross talk on the output signal can be summarized as:

- When C_y is set to zero, i.e. considering only the capacitive cross-talk on detector cell level, the output signal still has a single minimum at a frequency $\omega_o = 1/\sqrt{L_1 C_1}$. The resonance is shifted to lower frequencies as C_x increases (see table 4.1). Figure 4.6, shows the output signal for $C_x = 0.01 C_1$ (red curve), $C_x = 0.1 C_1$ (green curve), $C_x = 0.25 C_1$ (blue curve), $C_x = 0.5 C_1$ (dark yellow curve), $C_x = 0.75 C_1$ (light blue curve) as a function of frequency $\nu = \omega / 2\pi$.
- When C_x is set to zero, i.e. considering only the capacitive cross-talk on the readout chain level, in addition to the first minimum, a second minimum appears. While the position of the first minimum changes very slowly toward lower frequencies when C_y increases, the second minimum appears at lower frequencies (see table 4.1). Figure 4.7, shows the output signal for $C_y = 0.01 C_1$ (red curve), $C_y = 0.1 C_1$ (green curve), $C_y = 0.25 C_1$

C_1 (blue curve), $C_y = 0.5 C_1$ (dark yellow curve), $C_y = 0.75 C_1$ (light blue curve) as a function of frequency ν .

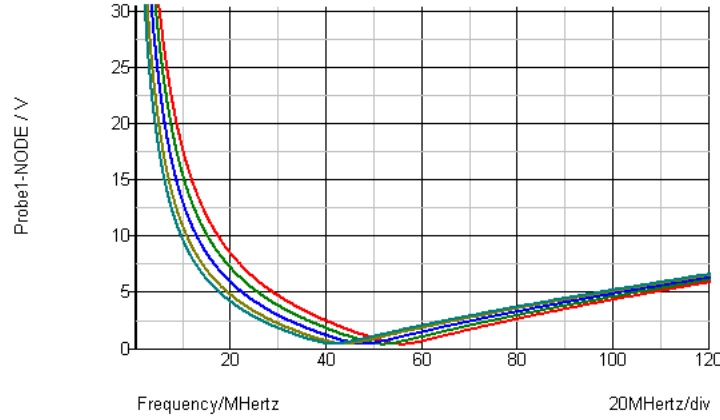


Fig. 4.6: Resonance curves for different C_x values in case of only one neighboring cell.

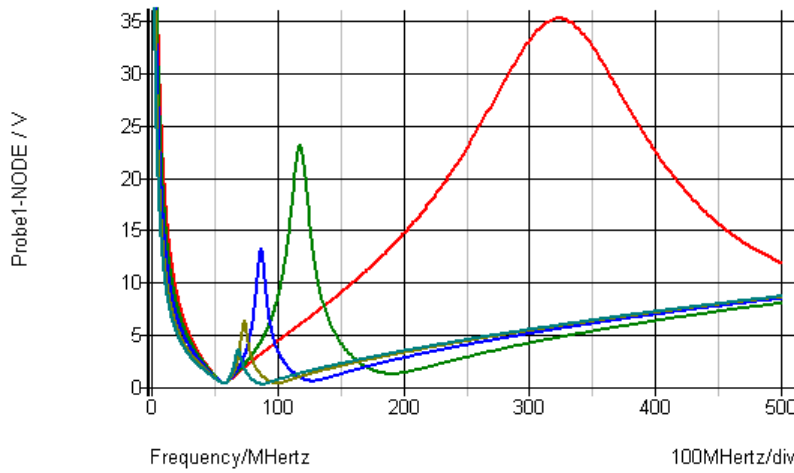


Fig. 4.7: Resonance curves for different C_y values in case of only one neighboring cell.

The second minimum appeared here can lead to a wrong value for LC (which is essential for pulse prediction), if one picked the wrong one. Thus to extract the right value for LC one must pick the minimum at lower frequency which could be shifted due to the effect of C_x . A correction for the shift arises due to C_x effect must be applied.

The situation becomes complicated if one considers the second order neighbor cells. The corresponding network is shown in figure 4.8 in which, the pulsed cell is represented by R_1 , L_1 and C_1 and its output is taken through the preamplifier R_6 . While the 1st order neighbors are represented by R_1 , L_2 , and C_2 , and R_2 , L_3 , and C_3 , the 2nd order neighbors are represented by R_7 , L_4 , and C_8 , and R_9 , L_5 , and C_9 . The C_x cross-talk contribution is represented by C_5 , C_4 , C_{10} , and C_{11} , while The C_y contribution is represented by C_6 , C_7 , C_{12} , and C_{13} .

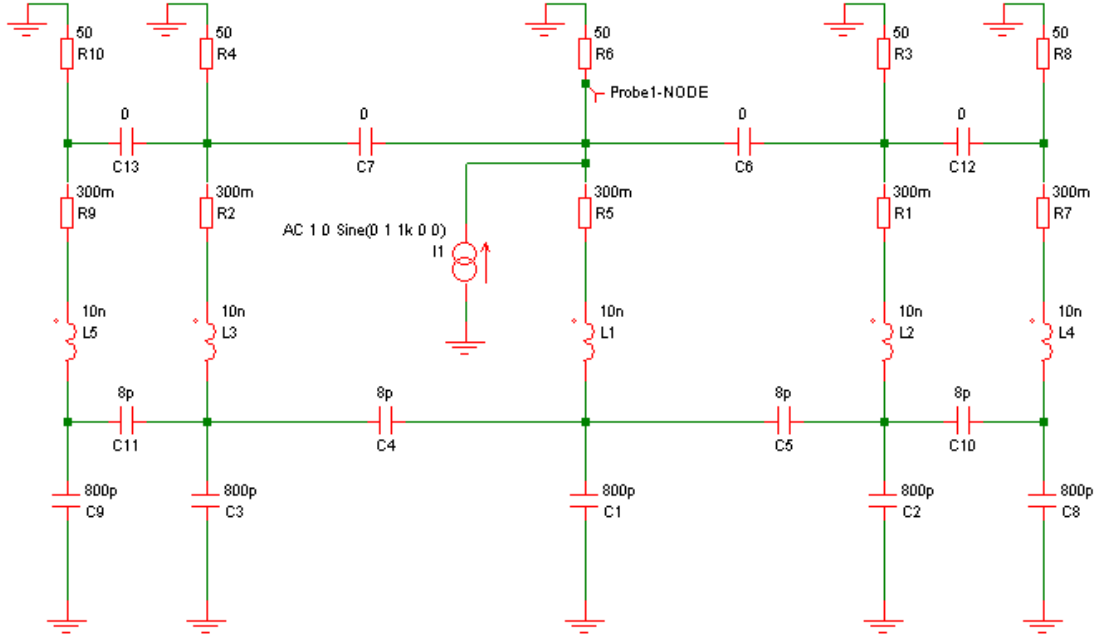


Fig. 4.8: Schematic of a cell with a capacitive cross talk with 4 neighboring cells, 2 on each side.

As in 1st order case we can select different values for capacitive cross talk and see the response of our network. The impact of cross talk on the output signal can be summarized as:

- When we set C_y to zero and give a value for C_x , the output signal still has a single minimum at a frequency $\omega_o = 1/\sqrt{L_1 C_1}$. The resonance is shifted to lower frequencies as C_x increases. But here the shift is slightly bigger than the 1st order case (see table 4.1). Figure 4.9, shows the output signal for $C_x = 0.01 C_1$ (red curve), $C_x = 0.1 C_1$ (green curve), $C_x = 0.25 C_1$ (blue curve), $C_x = 0.5 C_1$ (dark yellow curve), $C_x = 0.75 C_1$ (light blue curve) as a function of frequency ν .
- When we set C_x to zero and give a value for C_y , in addition to the first minimum and the second minimum which had appeared in the 1st order case a third minimum appear between the first and the second minima. While the position of the first minimum could be considered to be stable when the value of C_y changes (see table 4.1), the second and third minima are shifted to lower frequencies as C_y increases. Figure 4.10, shows the output signal for $C_y = 0.01 C_1$ (red curve), $C_y = 0.1 C_1$ (green curve), $C_y = 0.25 C_1$ (blue curve), $C_y = 0.5 C_1$ (dark yellow curve), $C_y = 0.75 C_1$ (light blue curve) as a function of frequency ν .

In general, as shown in table 4.1, there are no much variations in the position of the first minimum due to changes in C_y cross-talk contribution. Therefore, one can neglect changes due to C_y contributions considering only changes due to C_x contributions. Moreover, the frequency shift in the 1st minimum position due to C_x contribution in 1st order case (which considers only one neighbor) is comparable to that in the 2nd order case (which considers two neighbor). Thus, for simplicity we can consider only the 1st order case for frequency shifts in the first minimum position.

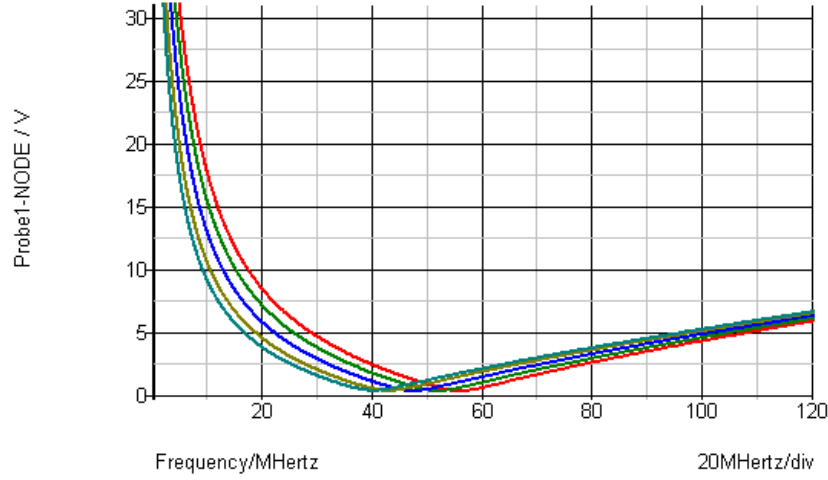


Fig. 4.9: Resonance curves for different C_x values in case of 4 neighboring cells (two on each side).

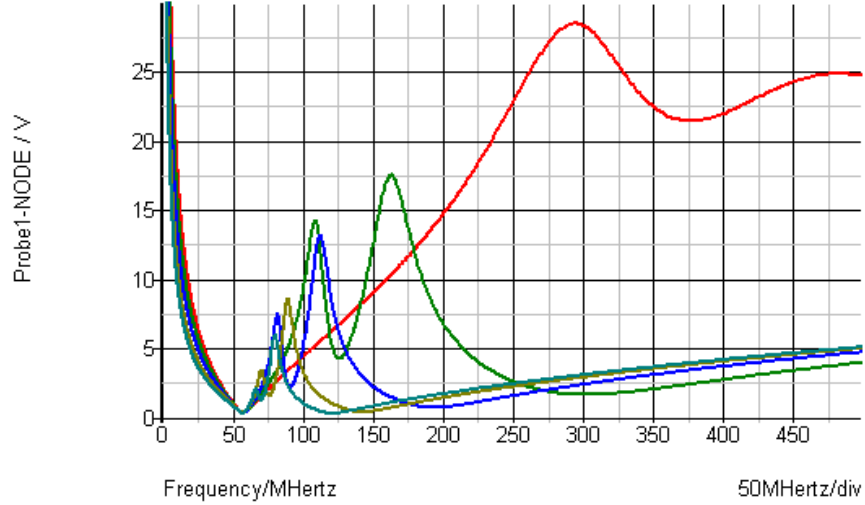


Fig. 4.10: Resonance curves for different C_y values in case of 4 neighboring cells (two on each side).

4.3.2 Adding cables

The above discussion neglects all the cable effects such as reflections and mutual induction. Considering these effects will not affect significantly the resonance position but it causes other minima appearing at lower and higher frequencies because outside the resonance region. The signal shape is sensitive to the impedance termination of the signal output. Because the signal cables have a characteristic impedance of 25Ω and the feedthrough cables of 33Ω a partial reflection takes place [24]. Considering these effects is beyond the scope of the current study. Cables effects on the output signal are considered in the network shown in figure 4.11. The left part of figure 4.11, represents the calibration circuit where the signal injection is done through a scanner (represented by $R_1 = 50 \Omega$) plugged on the feedthrough which is represented as T_1 (a 33Ω cable 5 ns long) then follows the calibration cable T_2 (a 50Ω cable 25 ns long) which bring the signal to the motherboard where the calibration resistance R_5 ($R_{Cali} = 1 \text{ k}\Omega$ for A and 500Ω for B

electrodes respectively) is plugged. Then the injected signal sees the detector as an rLC circuit, represented by R_4 in series with L_1 and C_1 . Then it goes through the signal cable T_3 (25 Ω 22 ns long) back to the feedthrough T_4 at the right part of figure 4.11. The signal is readout through a scanner R_5 . The capacitive cross-talk effect is represented by the capacitors C_{10} , and C_{12} for the C_x contribution and C_6 , and C_8 for the C_y contribution.

No. of neighbors	C_x/C	C_y/C	1 st v_o (MHz)	2 nd v_o (MHz)	3 rd v_o (MHz)
One neighbor	0.01	0	55.843162	--	--
	0.10	0	51.876421	--	--
	0.25	0	47.53024	--	--
	0.50	0	43.548179	--	--
	0.75	0	41.397108	--	--
	0	0.01	56.359873	647.097921	--
	0	0.10	56.100923	189.221292	--
	0	0.25	56.100923	126.75643	--
	0	0.50	56.100923	97.942223	--
	0	0.75	56.100923	86.09343	--
Two neighbors	0.01	0	55.843162	--	--
	0.10	0	51.63807	--	--
	0.25	0	47.311858	--	--
	0.50	0	42.753336	--	--
	0.75	0	39.899734	--	--
	0	0.01	56.359873	--	375.811447
	0	0.10	56.100923	301.279793	125.017268
	0	0.25	56.100923	192.739174	90.150887
	0	0.50	56.100923	141.5696	75.330353
	0	0.75	56.100923	119.941646	69.337791

Table 4.1: Minima positions in case of 1st and 2nd order neighboring cells for different values of C_x and C_y .

The lower part of figure 4.12 shows the output signal for the 1st order neighboring cells with cables effects from the network shown in figure 4.11 while the upper part shows that without any cable effects using the network shown in figure 4.5. Of course, this is because the total impedance of the network is much higher when cables are added. Comparing two curves with the same colour, one can see how the cables affect on the output signal. The red curves represent the output signals without any cross-talk ($C_x = C_y = 0$), comparing the two red curves we can see the wiggles at high frequencies and the flat part due to cable effect although the cables have no effect on the minimum position. The green curves show the output signal with only the C_x cross-talk contribution ($C_x = 0.4 C_1$ and $C_y = 0$) which shift the signal to lower frequency. The blue curves show the output signal with only the C_y cross-talk contribution ($C_x = 0$ and $C_y = 0.4 C_1$) which add a second minimum to the right of the main minimum. The black curves show the output signal with both the two cross-talk contributions ($C_x = 0.4 C_1$ and $C_y = 0.4 C_1$). In both cases, with and without cables, this signal shown in black is shifted due to C_x cross-talk contribution and has a second minimum due to C_y cross-talk contribution.

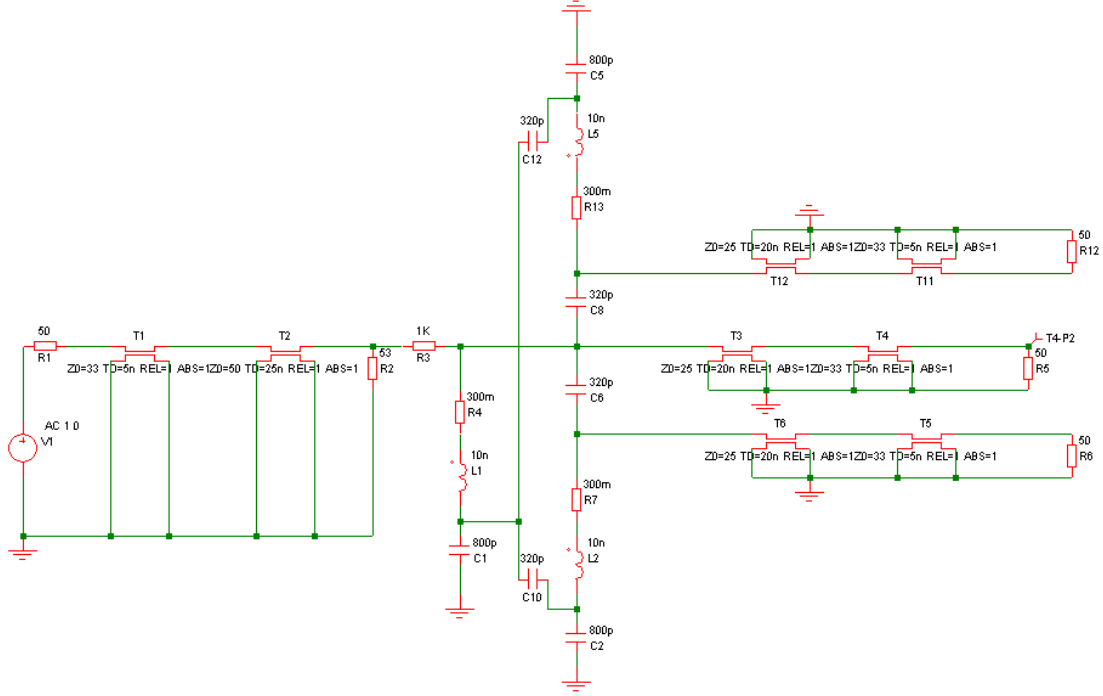


Fig. 4.11: Schematic of a cell with a capacitive cross talk with 2 neighboring cells, one on each side considering the cables effects.

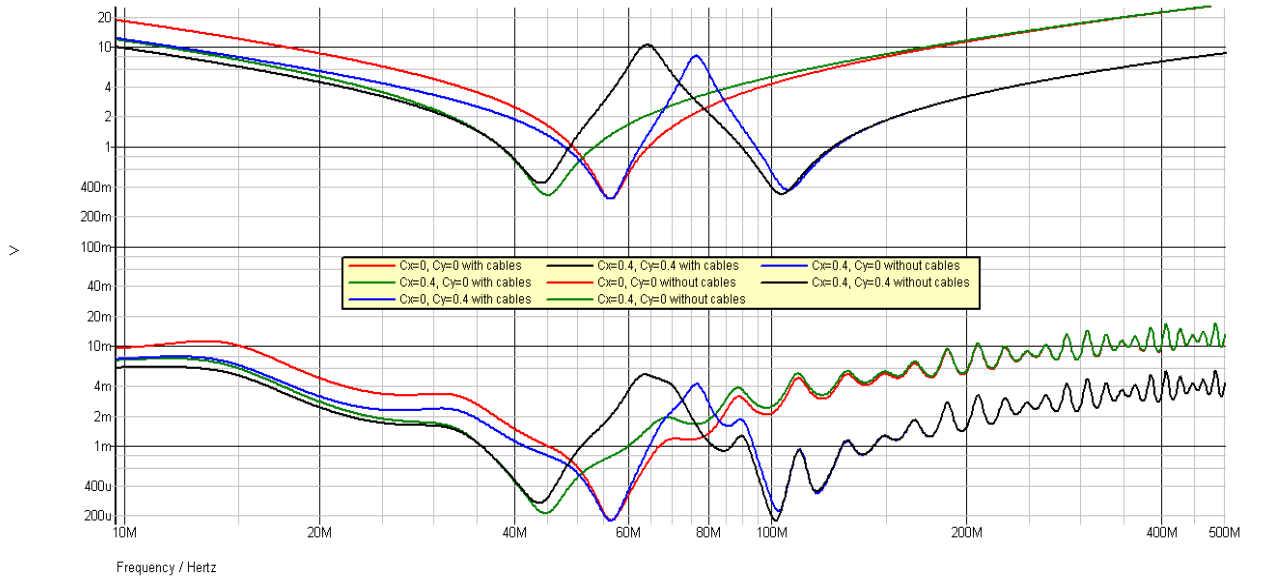


Fig. 4.12: Resonance curves for 1st order neighboring cells with and without cross-talk.

4.3.3 Estimation of C_x and C_y

Figure 4.13 shows the current out of the pulsed cell $I_C(C_x, C_y)$ while figure 4.14 shows the current out of the neighbor cell $I_{NC}(C_x, C_y)$ when $C_y = 0$, using the network shown in figure 4.5 where $C_d = C_1$, the LAr gap capacitance.

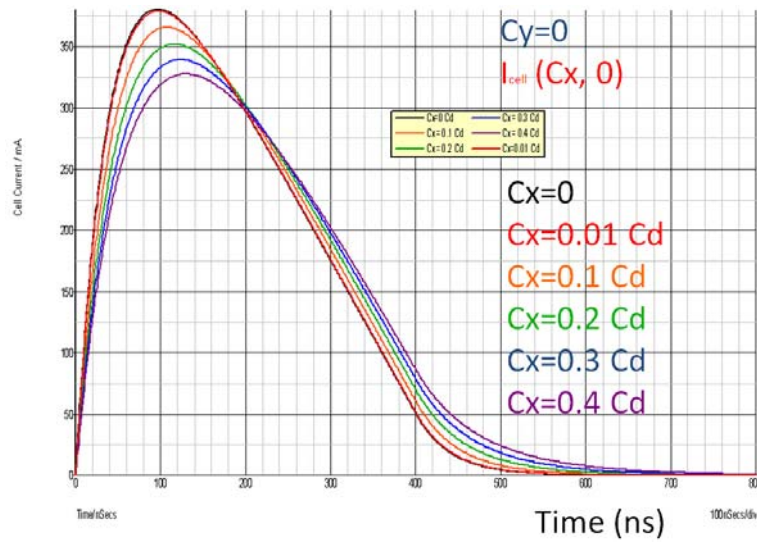


Fig. 4.13: Pulsed cell current as a function of C_x when $C_y = 0$.

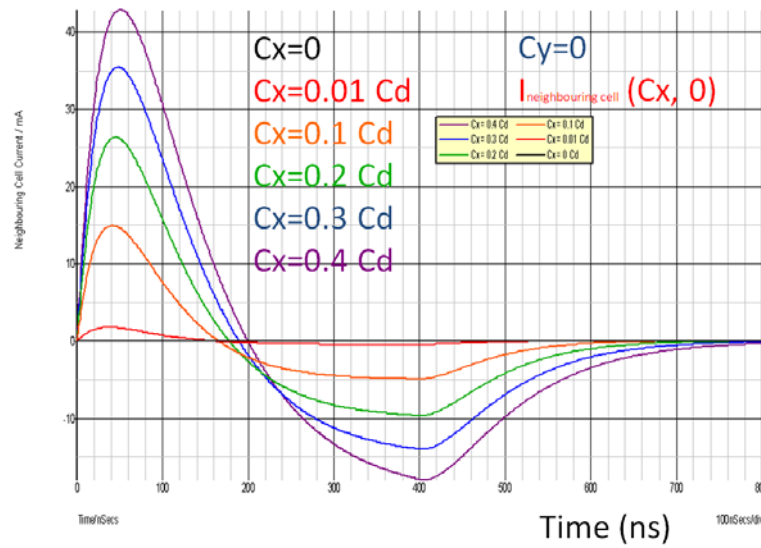


Fig. 4.14: Neighboring cell current as a function of C_x when $C_y = 0$.

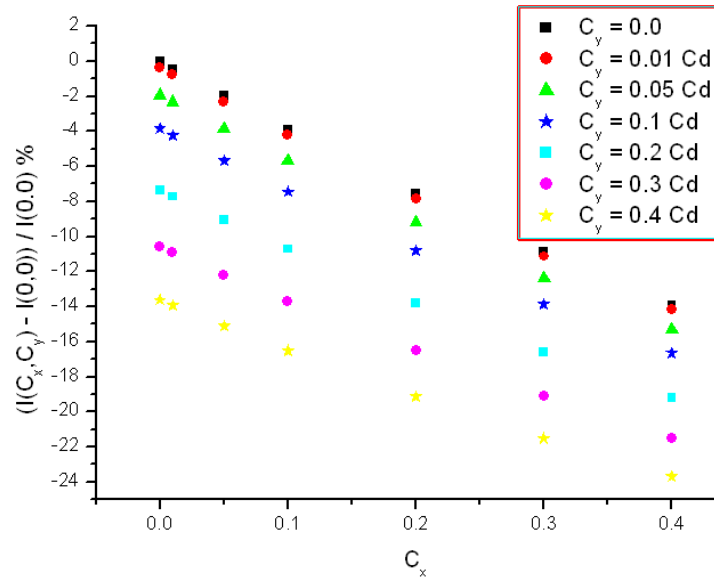


Fig. 4.15: The percentage of pulsed cell current change as a function of C_x and C_y .

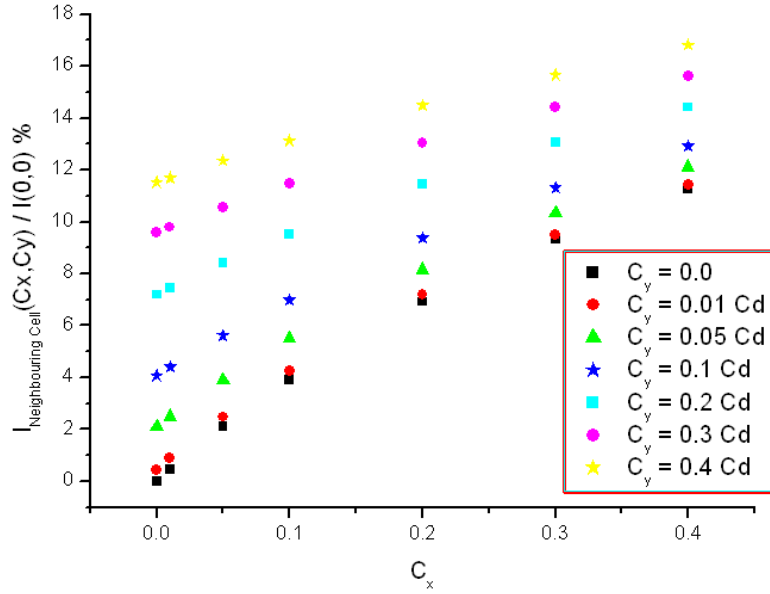


Fig. 4.16: The percentage of neighbor cell current as a function of C_x and C_y .

Figure 4.15 shows $\frac{I_C(C_x, C_y) - I_C(0,0)}{I_C(0,0)}\%$ as a function of C_x and C_y , while figure 4.16 shows $\frac{I_{NC}(C_x, C_y)}{I_C(0,0)}\%$ as a function of C_x and C_y . From [29] it is known that the strip-strip peak to peak capacitive cross-talk is about 7.2 % for 1st neighbor strip. Therefore from the results shown in figure 4.15 one can conclude that $C_x = C_y =]0.0, 0.2[$ Cd. The solutions where $C_x = 0.0$ and $C_y = 0.0$ are excluded. In this work the solution where $C_x = C_y = 0.1$ Cd is considered.

4.4 Analytical formulation of the capacitive cross-talk effects

In this section we will consider only the impact of the two cross-talk contributions on the output signal and will not consider the cable effect because it is very complicated to treat it mathematically moreover, as we already saw in the previous section, the cables have no effect on the main resonance.

4.4.1 First order neighboring cells

- Calibration current

In the network shown in figure 4.17 one can find the following expressions for the pulsed cell calibration current, I_C^{cali} and for the neighboring cell calibration current, I_{NC}^{cali}

$$I_C^{cali} = \frac{1}{3} \left\{ \frac{I_{inj}^{cali} (1 + sC(r + sL))}{1 + sC(r + sL) + sCZ_{PA}} \right\} + \frac{1}{3} \left\{ \frac{2I_{inj}^{cali} [1 + (C + 3C_X)s(r + sL)]}{1 + (C + 3C_X)s(r + sL) + sZ_{PA} [3(C_X + C_Y) + 9sC_X C_Y(r + sL) + C(1 + 3sC_Y(r + sL))]} \right\} \quad (4.9)$$

$$I_{NC}^{cali} = \frac{I_{inj}^{cali} sZ_{PA} \{C_Y(1 + sC(r + sL))^2 + C_X(1 + 3sC_Y(r + sL))(1 + sC(r + sL))\}}{(1 + sC(r + sL) + sCZ_{PA}) \{1 + (C + 3C_X)s(r + sL) + sZ_{PA} [3(C_X + C_Y) + 9sC_X C_Y(r + sL) + C(1 + 3sC_Y(r + sL))]\}} \quad (4.10)$$

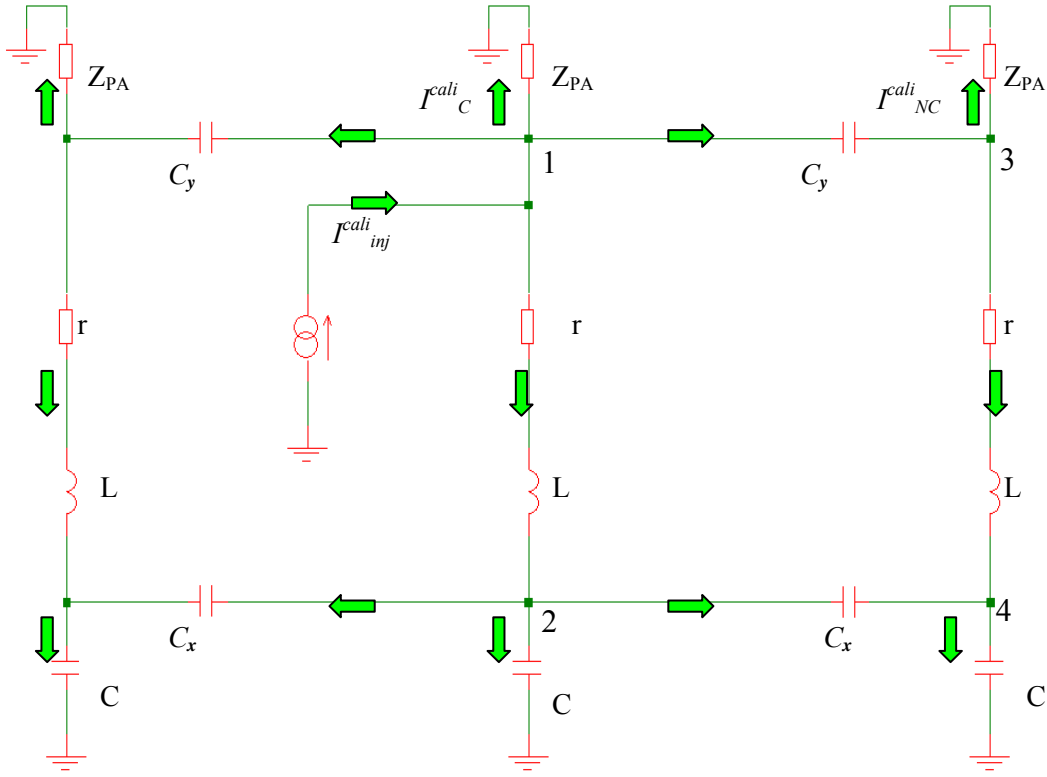


Fig. 4.17: The calibration current circuit with two neighboring cells, one on each side.

Then the output voltage at the preamplifier of the pulsed cell becomes;

$$V_{Out}^{cali} = I_C^{cali} Z_{PA} \quad (4.11)$$

The sum of the output voltages of the three cells is given by;

$$\sum V_{Out}^{cali} = (I_C^{cali} + 2I_{NC}^{cali}) Z_{PA} = \frac{I_{inj}^{cali} (1 + sC(r + sL)) Z_{PA}}{1 + sC(r + sL) + sCZ_{PA}} \quad (4.12)$$

The total impedance of the calibration circuit as seen by the injected calibration current is given by

$$Z_{cali}^{(1)} = \frac{Z_{PA}}{3} \left(\frac{1 + sC(r + sL)}{1 + sC(r + sL + Z_{PA})} \right) + \frac{Z_{PA}}{3} \left(\frac{2(1 + s(C + 3C_x)(r + sL))}{1 + 3sC_y Z_{PA} + sC(r + sL + Z_{PA} + 3sC_y Z_{PA}(r + sL)) + 3sC_x(r + sL + Z_{PA} + 3sC_y Z_{PA}(r + sL))} \right) \quad (4.13)$$

where the superscript (1) refers to the 1st order case (i.e. the 1st order neighbor). Figure 4.18 shows $Z_{cali}^{(1)}$ as a function of frequency $\nu = \omega / 2\pi$.

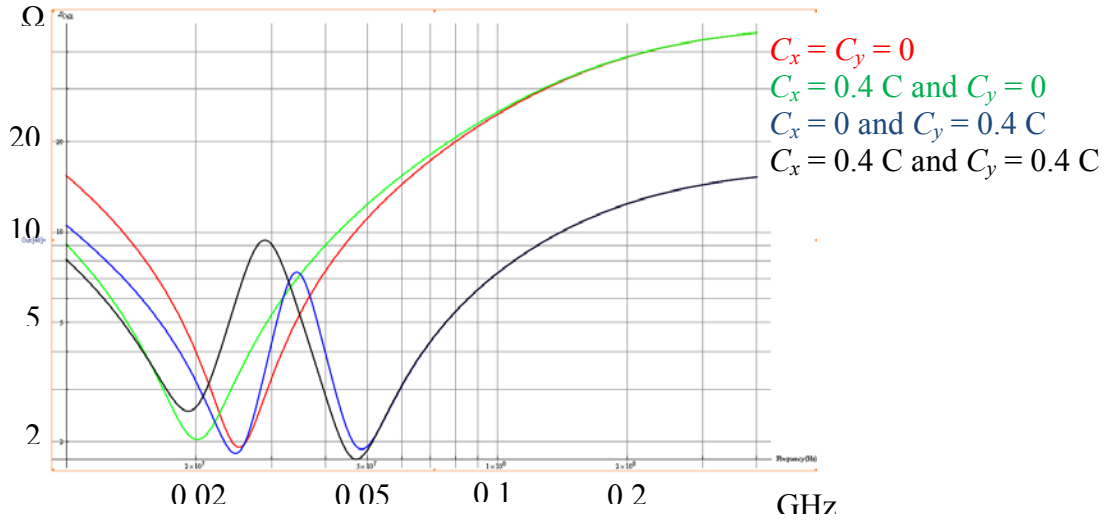


Fig. 4.18: $Z_{cali}^{(1)}$ as a function of frequency.

In figure 4.18 the red line represents the output signals without any cross-talk ($C_x = C_y = 0$), which has only one minimum as expected for a deaf cell which does not communicate with its neighbors. The green line shows the output signal with only the C_x cross-talk contribution ($C_x = 0.4 C$ and $C_y = 0$) which shift the signal to lower frequency as it has to be when we have only the C_x cross-talk contribution. The blue line shows the output signal with only the C_y cross-talk contribution ($C_x = 0$ and $C_y = 0.4 C$) which add a second minimum to the right of the main minimum and approximately does not touch the main minimum, which represents the behavior of C_y that shown by the simulator in the 1st order case. The black line shows the output signal with both the two cross-talk contributions ($C_x = 0.4 C$ and $C_y = 0.4 C$), which is shifted due to C_x cross-talk contribution and has a second minimum due to C_y cross-talk contribution. The function $Z_{cali}^{(1)}$ that is shown in figure 4.18 is exactly has the same shape as the upper part of figure 4.12 which is done using the simulator thus we have an analytical function which describes well the impact of cross-talk on the calibration signal in the resonance region.

- Physics current

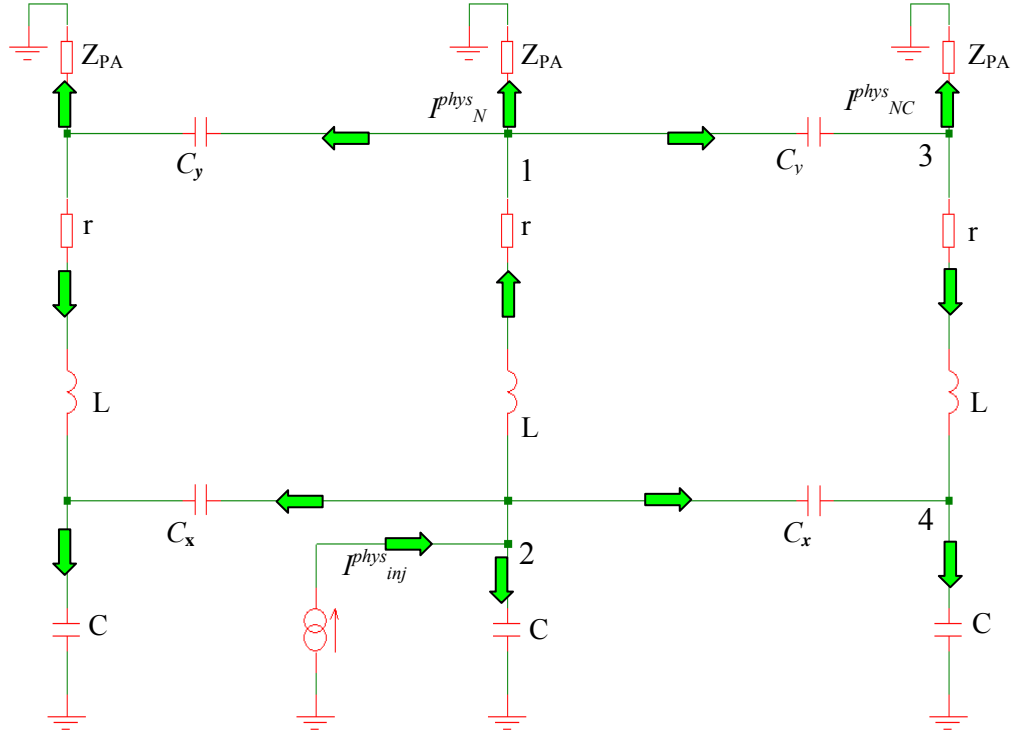


Figure 4.19: The physics current circuit with two neighboring cells, one on each side.

In the network shown in figure 4.19 one can find the following expressions for the pulsed cell physics current I_C^{phys} and for the neighboring cell physics current I_{NC}^{phys}

$$I_C^{phys} = \frac{I_{inj}^{phys}}{3} \left\{ \frac{1}{1 + sC(r + sL) + sCZ_{PA}} \right\} + \frac{I_{inj}^{phys}}{3} \left\{ \frac{2}{1 + s(C + 3C_X)(r + sL) + sZ_{PA}[3(C_X + C_Y) + 9sC_XC_Y(r + sL) + C(1 + 3sC_Y(r + sL))]} \right\} \quad (4.14)$$

$$I_{NC}^{phys} = \frac{I_{inj}^{phys} s \{ C_X(r + sL) + Z_{PA}(C_X + C_Y + srC_Y(C + 3C_X) + s^2LC_Y(1 + 3C_X)) \}}{(1 + sC(r + sL) + sCZ_{PA})[1 + s(C + 3C_X)(r + sL) + sZ_{PA}[3(C_X + C_Y) + 9sC_XC_Y(r + sL) + C(1 + 3sC_Y(r + sL))]]} \quad (4.15)$$

Then the output voltage at the preamplifier of the pulsed cell,

$$V_{out}^{phys} = I_C^{phys} Z_{PA} \quad (4.16)$$

and the summation of the output voltage of all the three cells is given by;

$$\sum V_{out}^{phys} = (I_N^{phys} + 2I_{NC}^{phys}) Z_{PA} = \frac{I_{inj}^{phys} Z_{PA}}{1 + sC(r + sL) + sCZ_{PA}} \quad (4.17)$$

Then going from calibration to physics pulse, the transfer function will be;

$$R = \frac{V_{Out}^{phys}}{V_{out}^{cali}} \quad (4.18)$$

Substitute equations (9) and (11) and then equations (14) and (16) into equation (18), one gets;

$$R = \{ I_{inj}^{phys} (1 + s(C + C_x)(r + sL) + s Z_{PA} (C + C_x + C_y + s r C_y(C + 3C_x) + s^2 L C_y(C + 3C_x))) \} / \\ \{ I_{inj}^{cali} ((1 + s C (r + sL))(1 + s(C + 3C_x)(r + sL)) + s (C_x + C_y + 3s C_x C_y (r + sL) + s C^2(r + sL) (1 + s C_y(r + sL)) + C (1 + s(r + sL) (2 C_y + 3 C_x (1 + s C_y(r + sL))))) Z_{PA}) \} \quad (4.19)$$

When one considers that there is no cross-talk between the cells, i.e. setting $C_x = C_y = 0$, equation 4.19 will be reduced to;

$$R = \frac{I_{inj}^{phys}(s)}{I_{inj}^{cali}(s)} \times \frac{1}{1 + srC + s^2 LC} \quad (4.20)$$

Equation 4.20 can be rewritten as;

$$I^{phys}(s) = I^{cali}(s) \times \underbrace{\frac{I_{inj}^{phys}(s)}{I_{inj}^{cali}(s)}}_{g^{exp \rightarrow tri}(s)} \times \underbrace{\frac{1}{1 + s\tau_r + s^2\tau_o^2}}_{g^{MB \rightarrow det}(s)} \quad (4.21)$$

which is the same as equation 4.2. Writing it in this form to emphasize on that the two signals (physics and calibration) differ in two reasons:

- (i) The two pulses have different injection shape. The physics pulse has a triangular current shape, whereas the injected calibration current has an exponential one.
- (ii) The two pulses are injected into two different locations.

All the effects due to the readout line, the preamplifier and the shaper (described by the parameter Z_{PA} , for simplicity) are common to both signals and cancel out when one takes the ratio. Dividing equation 4.17 by equation 4.12, one gets the ratio of the sums of the output voltages;

$$Ratio = \frac{\sum V_{Out}^{phys}}{\sum V_{Out}^{cali}} = \frac{I_{inj}^{phys}(s)}{I_{inj}^{cali}(s)} \times \frac{1}{1 + srC + s^2 LC} \quad (4.22)$$

which again reproduces the same function as that one without any cross-talk. Therefore one can remove the influence of the cross-talk, when going from physics to calibration pulse, if one takes

the ratio of the sums of the pulses of the pulsed cell and its neighbors for physics and calibration pulses. However the extraction of ω_o from the resonance curve is biased for $C_x \neq 0$, i.e. if $C_x = 0$ but $C_y \neq 0$, $\omega_o = 1/\sqrt{LC}$ is still the minimum of the curve. Only if $C_x \neq 0$, then one gets a wrong estimate of the minimum.

4.4.2 Second order neighboring cells

Throughout this subsection care must be taken because the currents here have deferent expirations than that derived in the in the case of first order although they will be denoted with the same symbols. There will be no confusion between the two cases since each case is treated separately.

- Calibration current

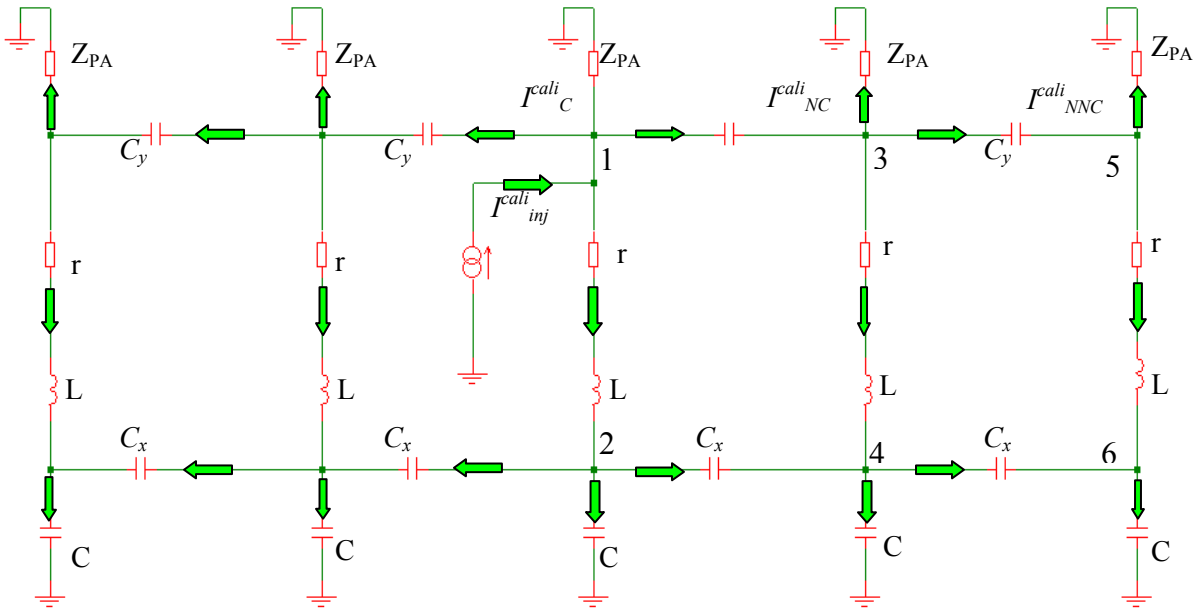


Figure 4.20: The calibration current circuit with 4 neighboring cells, two on each side.

In the network shown in figure 4.20 one can find expressions for the pulsed cell calibration current I_C^{cali} , for the neighboring cell physics current I_{NC}^{cali} and for the next to neighboring cell calibration current I_{NNC}^{cali} and similarly the voltage out of the pulsed cell is,

$$V_{Out}^{cali(2)} = I_C^{cali} Z_{PA} \quad (4.23)$$

and the summation of the voltage out of the pulsed cell and its neighbors, in this case becomes;

$$\sum V_{Out}^{cali(2)} = (I_C + 2I_{NC} + 2I_{NNC})Z_{PA} = \frac{I_{inj}^{cali}(1 + sC(r + sL))Z_{PA}}{1 + sC(r + sL) + sCZ_{PA}} \quad (4.24)$$

The total impedance of the calibration circuit as seen by the injected calibration current is given by;

$$Z_{cali}^{(2)} = \frac{V_{Out}^{cali(2)}}{I_{inj}^{cali}} = \frac{\{Z_{PA}((1 + sC(r + sL))(1 + s(r + sL)(sC^2(r + sL) + 5C_x(1 + sC_x(r + sL)) + C(2 + 5sC_x(r + sL)))) + sZ_{PA}(3(C_x + C_y) + s^2C^3(r + sL)^2(2 + 3sC_y(r + sL)) + 3sC_x(r + sL)(5C_y + C_x(2 + 5sC_y(r + sL))) + sC^2(r + sL)(4 + s(r + sL)(9C_y + 5C_x(2 + 3sC_y(r + sL)))) + C(2 + s(r + sL)(9C_y + C_x(13 + 5s(r + sL)(6C_y + C_x(2 + 3sC_y(r + sL)))))) + s(C^2 + C_xC_y(2 + 5sC_y(r + sL)) + C_x^2(1 + 5sC_y(r + sL)(1 + sC_y(r + sL))) + sC^3(r + sL)(1 + sC_y(r + sL)(3 + sC_y(r + sL))) + C(3C_y(1 + C_y(r + sL)) + 5sC_x^2(r + sL)(1 + sC_y(r + sL)(3 + sC_y(r + sL))) + C_x(3 + sC_y(r + sL)(17 + 10sC_y(r + sL)))) + C^2(1 + s(r + sL)(3C_y(2 + sC_y(r + sL)) + 5C_x(1 + sC_y(r + sL)(3 + sC_y(r + sL))))))Z_{PA})\}}{(1 + sC(r + sL + Z_{PA}))(1 + s(r + sL)(sC^2(r + sL) + 5C_x(1 + C_x s(r + sL)) + C(2 + 5sC_x(r + sL))) + sZ_{PA}(5(C_x + C_y) + sC^2(r + sL)(2 + 5sC_y(r + sL)) + 5sC_x(r + sL)(5C_y + C_x(2 + 5sC_y(r + sL))) + C(2 + 5s(r + sL)(2C_y + C_x(2 + 5sC_y(r + sL)))) + s(C^2(1 + 5sC_y(r + sL)(1 + sC_y(r + sL))) + 5C(C_y + 2sC_y^2(r + sL) + C_x(1 + 5sC_y(r + sL)(1 + sC_y(r + sL)))) + 5(C_y^2 + C_xC_y(2 + 5sC_y(r + sL)) + C_x^2(1 + 5sC_y(r + sL)(1 + sC_y(r + sL))))))Z_{PA})\}}$$

(4.25)

where the superscript (2) refers to the 2nd order case (i.e. the 2nd order neighbors). Figure (4.21) shows $Z_{cali}^{(2)}$ as a function of frequency $\nu = \omega / 2\pi$.

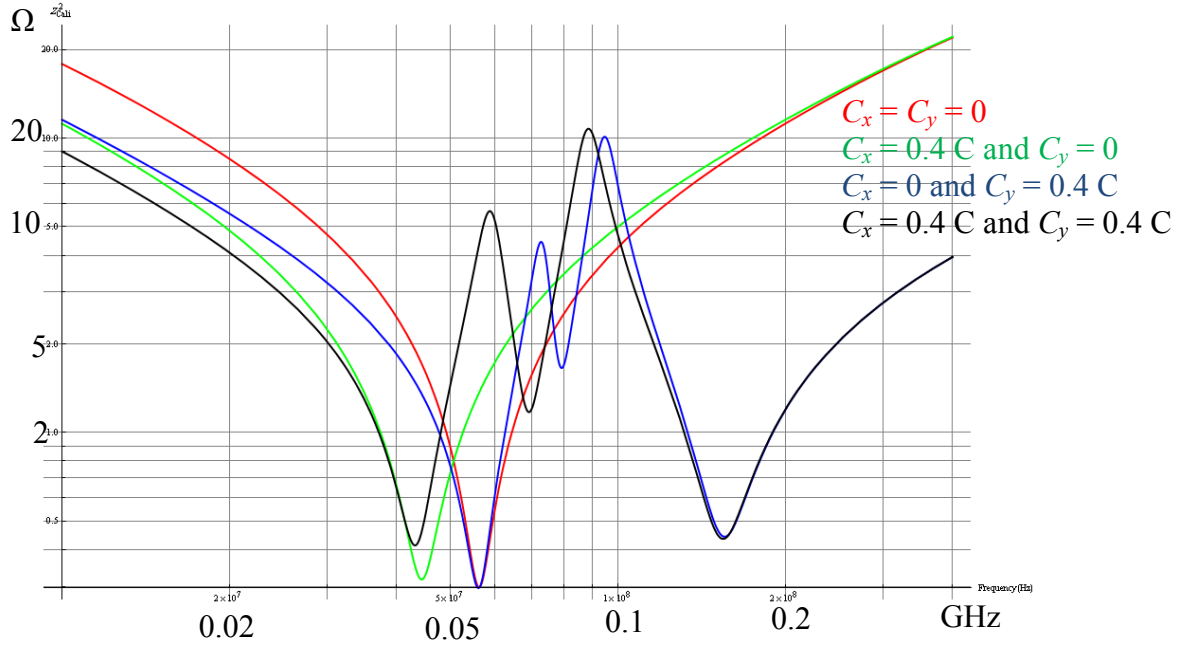


Fig 4.21: $Z_{cali}^{(2)}$ as a function of frequency

As in the previous case, in figure (4.21) the red line represents the output signals without any cross-talk ($C_x = C_y = 0$), which has only one minimum as expected for a deaf cell which does not communicate with its neighbors. The green line shows the output signal with only the C_x cross-talk contribution ($C_x = 0.4 C$ and $C_y = 0$) which shift the signal to lower frequency as it has to be when we have only the C_x cross-talk contribution. The blue line shows the output signal with only

the C_y cross-talk contribution ($C_x = 0$ and $C_y = 0.4 C$) which add a second and a third minima to the right of the main minimum and approximately does not touch the main minimum, the position of the 3rd minimum is in the middle between the 1st and the second minimum which had appeared in the 1st order approximation. This represents the behavior of C_y that shown by the simulator in the 2nd order case. The black line shows the output signal with both the two cross-talk contributions ($C_x = 0.4 C$ and $C_y = 0.4 C$), which is shifted due to C_x cross-talk contribution and has a 2nd and a 3rd minimum due to C_y cross-talk contribution. The function $Z_{Cali}^{(2)}$ that is shown in figure (4.16) shows exactly the same behavior as described in section 4.3 for the 2nd order case. Again we have an analytical function which describes well the impact of cross-talk on the calibration signal in the resonance region up to the 2nd order case.

Comparing the two green lines in 4.18 and 4.21, one conclude that there is no much variation in the frequency shift which comes from the C_x cross-talk contribution when we use the 2nd order neighbor instead of the 1st order, that is consistence with the discussion in section 4.3 (see table 4.1). Thus, the 1st order case can be used as a good approximation.

- Physics current

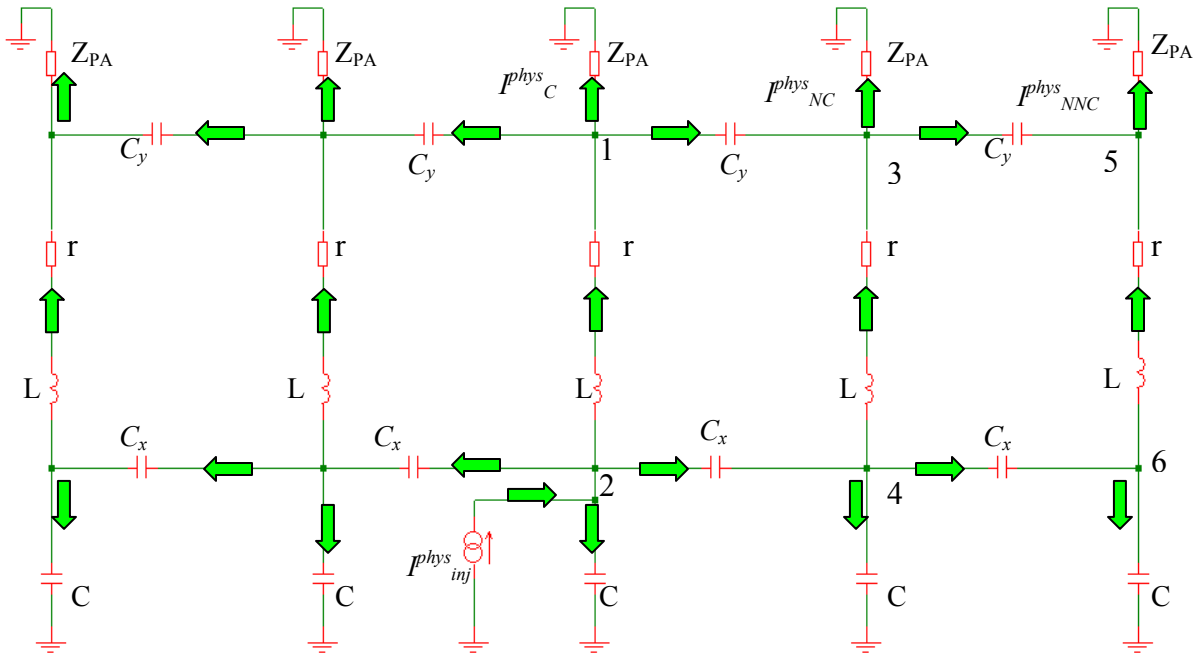


Fig. 4.22: The physics current circuit with 4 neighboring cells, two on each side.

Using the network shown in figure 4.22 one can find expressions for the pulsed cell physics current I_C^{phys} , for the neighboring cell physics current I_{NC}^{phys} and for the next to neighboring cell physics current I_{NNC}^{phys} . The voltage out of the pulsed cell is,

$$V_{Out}^{phys(2)} = I_C^{phys} Z_{PA} \quad (4.26)$$

while the summation of the voltage out of the pulsed cell and its neighbors;

$$\sum V_{Out}^{phys(2)} = (I_C^{phys} + 2I_{NC}^{phys} + 2I_{NNC}^{phys})Z_{PA} = \frac{I_{inj}^{phys} Z_{PA}}{1 + sC(r + sL) + sCZ_{PA}} \quad (4.27)$$

Then going from physics to calibration pulse, the transfer function will be;

$$R = \frac{V_{Out}^{phys(2)}}{V_{Out}^{cali(2)}} \quad (4.28)$$

$$R = \{ I_{inj}^{phys} (1 + s(r + sL)(sC^2(r + sL) + C_x(3 + sC_x(r + sL)) + C(2 + 3sC_x(r + sL))) + sZ_{PA}(3(C_x + C_y) + sC^2(r + sL)(2 + 3sC_y(r + sL)) + sC_x(r + sL)(11C_y + C_x(2 + 5sC_y(r + sL))) + C(2 + s(r + sL)(6C_y + C_x(6 + 11sC_y(r + sL)))) + s(C_y^2 + C_xC_y(2 + 5sC_y(r + sL)) + C_x^2(1 + 5sC_y(r + sL)(1 + sC_y(r + sL))) + C^2(1 + sC_y(r + sL)(3 + sC_y(r + sL))) + C(C_y(3 + 2sC_y(r + sL)) + C_x(3 + sC_y(r + sL)(11 + 5sC_y(r + sL)))))) Z_{PA}) \} / \{ I_{inj}^{cali} ((1 + sC(r + sL))(1 + s(r + sL)(sC^2(r + sL) + 5C_x(1 + sC_x(r + sL)) + C(2 + 5sC_x(r + sL)))) + sZ_{PA}(3(C_x + C_y) + s^2C^3(r + sL)^2(2 + 3sC_y(r + sL)) + 3sC_x(r + sL)(5C_y + C_x(2 + 5sC_y(r + sL))) + sC^2(r + sL)(4 + s(r + sL)(9C_y + 5C_x(2 + 3sC_y(r + sL)))) + C(2 + s(r + sL)(9C_y + C_x(13 + 5s(r + sL)(6C_y + C_x(2 + 3sC_y(r + sL)))))) + s(C_y^2 + C_xC_y(2 + 5sC_y(r + sL)) + C_x^2(1 + 5sC_y(r + sL)(1 + sC_y(r + sL))) + sC^3(r + sL)(1 + sC_y(r + sL)(3 + sC_y(r + sL))) + C(3C_y(1 + sC_y(r + sL)) + 5sC_x^2(r + sL)(1 + sC_y(r + sL)(3 + sC_y(r + sL))) + C_x(3 + sC_y(r + sL)(17 + 10sC_y(r + sL)))) + C^2(1 + s(r + sL)(3C_y(2 + sC_y(r + sL)) + 5C_x(1 + sC_y(r + sL)(3 + sC_y(r + sL)))))) Z_{PA}) \} \quad (4.29)$$

When we neglect C_x and C_y ,

$$R = \frac{I_{inj}^{phys}}{I_{inj}^{cali} (1 + sC(r + sL))} \quad (4.30)$$

Tacking the physics to calibration ratio of the sums of all the output currents, we get;

$$Ratio = \frac{\sum V_{Out}^{phys(2)}}{\sum V_{Out}^{cali(2)}} = \frac{I_{inj}^{phys}}{I_{inj}^{cali} (1 + sC(r + sL))} \quad (4.31)$$

The function that transfer the physics current to calibration current, has no cross-talk terms if one took the ratio of the sums of the output voltage of the pulsed cell and its neighboring cells as in the case of the 1st order this of course due to the conservation of the number of electrons.

4.4.3 Measurement of the LC parameter

As shown in section 4.3, the position of the 1st minimum is shifted to frequencies lower than the natural frequency $\omega_o = 1/\sqrt{LC}$ due to the C_x cross-talk contribution. The variation in the 1st minimum position due to C_y contribution is very small and could be neglected. Moreover the variations due to the 2nd order neighbor are also very small and could be neglected. Thus to determine the position of the 1st minimum, hence measurement of the LC parameter, it is

sufficient to consider only C_x contribution while sitting C_y to zero and use only the first order case.

In figure 4.19 if C_y is neglected, C should be replaced by $C + \frac{2}{1/C + 1/C_x}$ and the 1st minimum will be shifted to a frequency $\omega_{ox} = 1/\sqrt{L\left(C + \frac{2}{1/C + 1/C_x}\right)}$. Thus in LAr EMC strips where the capacitive cross-talk effects are considerably high, it is important to consider the minimum is at ω_{ox} and not at ω_o when extracting τ_o as described in section 4.2.2.

No. of neighbors	C_x/C	1 st ν_o (MHz) simulator	1 nd $\nu_{ox} = \omega_{ox}$ (MHz)
One neighbor	0.01	55.843162	55.720783
	0.10	51.876421	51.7606599
	0.25	47.53024	47.556635
	0.50	43.548179	43.586376
	0.75	41.397108	41.290722

Table 4.2: 1st minimum position in case of 1st order neighboring cells for different values of C_x and $C_y=0$ using the simulator ν_o and the approximate solution ν_{ox} .

Table 4.2 shows a comparison of the 1st minimum position in 1st ordered neighboring cells case obtained by using the circuit simulator ν_o and that obtained by replacing C by $C + \frac{2}{1/C + 1/C_x}$.

4.5 Impact of capacitive cross-talk on a single cell energy measurement

Due to the existence of capacitive cross-talk some of the pulsed cell current runs to the neighboring cells this lead to a decrease in cell current. Thus the factor M_{phys}/M_{cali} , which is used to correct the ramp factors for the difference between the calibration and physics signal heights, is changed due to the capacitive cross-talk that makes an error in reconstructing the energy content of a single cell (see section 3.6).

Using Mathematica 6.0 [31] M_{phys} and M_{cali} are determined by finding the maxima of the physics signal $I^{phys}(t)$ (equation 4.3) and of the calibration signal in time domain $I^{cali}(t) = L^{-1}\{I^{cali}(s)\}$ (equation 4.6), respectively. The percentage of relative energy change due to capacitive cross-talk can be determined from;

$$\frac{\Delta E}{E} \% = \frac{\left[\frac{1}{M_{phys}/M_{cali}} \right]_{C_x=0.1C} - \left[\frac{1}{M_{phys}/M_{cali}} \right]_{C_x=0}}{\left[\frac{1}{M_{phys}/M_{cali}} \right]_{C_x=0}} \% \quad (4.32)$$

which is found to be around 0.3% for the assumption that $C_x = C_y = 0.1 C$. Figure 4.23 shows $(\Delta E / E)\%$ as a function of η_{cell} at $\phi_{cell} = 30^\circ$. This is a small effect which can be corrected when a 0.1 % accuracy of energy content of a LAr cell is needed.

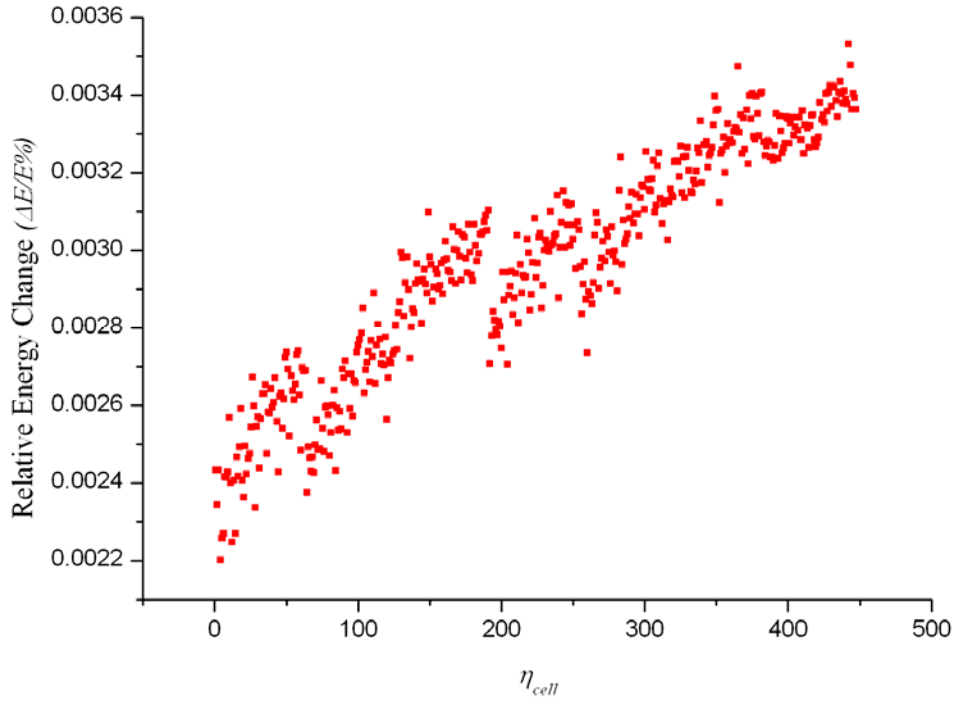


Fig. 4.23: the relative energy change due to capacitive cross-talk in LAr strips as a function of η_{cell} .

Conclusion

It is now understood that, in addition to the variations in signal response function due to the geometry of the LAr electromagnetic calorimeter, EMC. The signal response function is shifted also due to the capacitive coupling (capacitive cross-talk) between the front compartment (strips) of the LAr EMC of the level of the LAr gap. This leads to a change in the frequency of maximal response (ω_o). There is also a small effect coming from capacitive cross-talk on the level of the read-out chain. A mathematical expression of the capacitive cross-talk was given. The relative change in the energy content of a single cell, $(\Delta E/E) \%$, is always less than 0.3 % for reasonable estimates of the capacitive couplings at both levels. This effect will need to be accounted for to reach precision of 0.1% in the energy measurement in LAr EMC strips.

Acknowledgments

I would like to thank a lot Prof. Alain Blondel for giving me the chance to be one of University of Geneva ATLAS LAr group. Although he has a very tight schedule, he always was there when support is needed both in work-related problems as well as others.

I would like to particularly thank Martin Aleksa who introduces me to the ATLAS EMC community. He was always patient in answering my questions.

Many and special thanks to Arno Straessner for his help and support most of the time whatever my problem is he is always there and ready to find a solution.

I would like to thank a lot Marco Delmastro for helpful discussions and addressing a large part of this study.

At last but not least I would like to thank all University of Geneva ATLAS group people in particular Prof. Allan Clark, Andrew Hamilton and others.

Bibliography

- [1] The Large Hadron Collider, Technical Report CERN/AC/95-05, CERN, 1995.
- [2] LHC web page: <http://lhc.web.cern.ch/lhc/>
- [3] N.V. Krasnikov, V.A. Matveev. Search for standard Higgs boson at supercolliders. *Phys. Part. Nucl.*, 31, 2000.
- [4] G. Altarelli. The Standard Model and Beyond. *Nucl. Phys. B, Proc. Suppl.*, 75A, 1999.
- [5] F. Gianotti. Precision physics at LHC. ATLAS Internal Note, ATL-PHYS-99-001, 1999.
- [6] The ATLAS collaboration, Detector and Physics performances Technical Design Report. Technical Report CERN/LHCC/99-14 and 99-15, CERN, 1999.
- [7] The ATLAS Collaboration, The ATLAS Experiment at the CERN Large Hadron Collider, *JINST* **3** (2008) S08003.
- [8] The ATLAS collaboration, High{Level Triggers, DAQ and DCS Technical Design Report. Technical Report CERN/LHCC/2000-17, CERN, 2000.
- [9] Particle Data Group, Review of Particle Physics, *Physical Review D*, 2007.
- [10] R.Wigmans, *Calorimetry: EnergyMeasurement in Particle Physics*, Clarendon Press, Oxford, 2000.
- [11] Aubert, B. et. al, Construction, assembly and tests of the ATLAS electromagnetic barrel calorimter, CERN-PH-EP/2005-034, *Nucl. Instrum. Methods Phys.*, A558 (2006) 388-418.
- [12] M.L. Andrieux et al., Construction and test of the first two sectors of the ATLAS barrel liquid argon presampler, *Nucl. Instrum.Methods A* **479** (2002) 316–333.
- [13] J. Ban et al., ATLAS liquid argon calorimeter back end electronics, *JINST* **2** (2007) P06002.
- [14] E. Fullana et al., Digital Signal Reconstruction in the ATLAS Hadronic Tile Calorimeter, *IEEE Trans. Nucl. Sci.* Vol. 53, No. 4 (2006).
- [15] M. Aleksa et al. 2004 ATLAS Combined Testbeam: Computation and Validation of the Electronic Calibration Constants for the Electromagnetic Calorimeter. ATLAS Internal Note, ATL-LARG-PUB-2006-003, 2006.
- [16] W. E. Cleland, E.G. Stern, Signal Processing considerations for liquid ionization calorimeters in a high rate environment, *Nuclear Instruments and Methods in Physics Research A* 338 (1994) 467-497.
- [17] G. Graziani, Linearity of the response to test beam electrons for EM Barrel module P13, ATL-LARG-2004-001, 2004.

- [18] W. Walkowiak, Drift Velocity of Free Electrons in Liquid Argon, Atlas internal note ATL-LARG-99-008, 1999.
- [19] F. Hubaut, B. Laforge, D. Lacour, F. Orsini. Test beam Measurement of the Crosstalk in the EM Barrel Module 0. ATLAS Internal Note, ATL-LARG-2000-007, 2000.
- [20] M. Delmastro, Energy reconstruction and calibration algorithms for the ATLAS electromagnetic calorimeter, PhD-Thesis at the University of Milano, 2002.
- [21] R. L. Chase, C. de la Taille, J. P. Richer, N. Seguin-Moreau. A fast monolithic shaper for the ATLAS e.m. calorimeter. In Proc. 5th International Conference on Calorimetry in High-energy Physics, 1994.
- [22] M. Citterio, M. Delmastro and M. Fanti. A study of the electrical properties and of the signal shapes in the ATLAS Liquid Argon Accordion Calorimeter using a hardware model. ATLAS Internal Note, ATL-LARG-2001-018, 2001.
- [23] L. Neukermans, P. Perrodo and R. Zitoun. Understanding the electromagnetic barrel pulse shapes and the absolute electronic calibration. ATLAS Internal Note, ATL-LARG-2001-008, 2001.
- [24] S. Baffioni et al., Electrical measurements on the Atlas electromagnetic barrel calorimeter. ATLAS Internal Note, ATL-LARG-PUB-2007-005, 2007.
- [25] W. Willis and V. Radeka. Liquid Argon ionization chamber as a total absorption detector. NIM A, 120, 1974.
- [26] J. Colas et al. The LAr calorimeter calibration board. ATLAS Internal Note, ATL-LARG-2000-006, 2000.
- [27] C. De La Taille. ATLAS LAr electronics chain. Talk presented at the 1st ATLAS LAr Signal Reconstruction Workshop, CERN, July 7th, 2001.
- [28] D. Banfi, M. Delmastro and M. Fanti, Cell response equalization of the ATLAS electromagnetic calorimeter without the direct knowledge of the ionization signals. ATLAS Internal Note, SN-ATLAS-2005-054, 2005.
- [29] http://lpsc.in2p3.fr/atlas/labbe/BP3C/Xtalk/results_strip.php
- [30] P. Teixeira-Dias et al., Higgs boson searches at LEP. International Europhysics Conference on High Energy Physics, 19-25 July; Manchester, UK, (Preprint hep-ex/0804.4146).
- [31] <http://reference.wolfram.com/mathematica/guide/Mathematica.html>